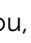





## PAPER

[View Article Online](#)  
[View Journal](#) | [View Issue](#)Cite this: *J. Mater. Chem. B*,  
2024, 12, 158Photothermal synergistic nitric oxide controlled  
release injectable self-healing adhesive hydrogel  
for biofilm eradication and wound healing†Weiling Peng,<sup>a</sup> Lixia Li,<sup>a</sup> Yu Zhang,<sup>a</sup> Haibing Su,<sup>a</sup> Xiaohu Jiang,<sup>a</sup> Haimeng Liu,<sup>a</sup>  
Xiaohua Huang, <sup>\*a</sup> Li Zhou, <sup>a</sup> Xing-Can Shen <sup>b</sup> and Chanjuan Liu <sup>\*a</sup>

The development of injectable self-healing adhesive hydrogel dressings with excellent bactericidal activity and wound healing ability is urgently in demand for combating biofilm infections. Herein, a multifunctional hydrogel (QP/QT-MB) with near-infrared (NIR) light-activated mild photothermal/gaseous antimicrobial activity was developed based on the dynamic reversible borate bonds and hydrogen bonds crosslinking between quaternization chitosan (QCS) derivatives alternatively containing phenylboronic acid and catechol-like moieties in conjunction with the *in situ* encapsulation of BNN6-loaded mesoporous polydopamine (MPDA@BNN6 NPs). Given the dynamic reversible cross-linking feature, the versatile hybrid hydrogel exhibited injectability, flexibility, and rapid self-healing ability. The numerous phenylboronic acid and catechol-like moieties on the QCS backbone confer the hydrogel with specific bacterial affinity, desirable tissue adhesion, and antioxidant stress ability that enhance bactericidal activity and facilitate the regeneration of infection wounds. Under NIR irradiation, the QP/QT-MB hydrogels exhibited a desirable mild photothermal effect and NIR-activity controllable NO delivery, combined with the endogenous contact antimicrobial activity of hydrogel, contributing jointly to induce dispersal of biofilms and disruption of the bacterial plasma membranes, ultimately leading to bacteria inactivation and biofilm elimination. *In vivo* experiments demonstrated that the fabricated QP/QT-MB hydrogel platform was capable of inducing efficient eradication of the *S. aureus* biofilm in a severely infected wound model and accelerating infected wound repair by promoting collagen deposition, angiogenesis, and suppressing inflammatory responses. Additionally, the QP/QT-MB hydrogel demonstrated excellent biocompatibility *in vitro* and *in vivo*. Collectively, the hydrogel (QP/QT-MB) reveals great potential application prospects as a promising alternative in the field of biofilm-associated infection treatment.

Received 2nd September 2023,  
Accepted 21st November 2023

DOI: 10.1039/d3tb02040a

[rsc.li/materials-b](https://rsc.li/materials-b)

## Introduction

Bacterial infections cause serious secondary damage to wounds and hinder wound-healing processes, leading to non-healing infected wounds and severe complications.<sup>1</sup> Wound dressings that can combat microorganism infections and modulate the wound repair process are critical for wound management. At present, wound dressings have evolved from traditional cotton

and gauze to sponges,<sup>2</sup> semipermeable membranes, hydrogels,<sup>3</sup> micro/nanofibers,<sup>4</sup> and other functional dressings. Hydrogel dressings emerge as promising candidates for effective wound management due to their high water content, maintenance of a moist wound environment, three-dimensional porous structure,<sup>5</sup> ability to permeate oxygen, and tissue exudate absorption.<sup>6</sup> Nevertheless, conventional hydrogel dressings exhibit limited antimicrobial activity, relying on external antibiotics to enhance their antimicrobial abilities.<sup>7</sup> Moreover, bacteria in the wound beds tend to aggregate as multicellular communities and are embedded in self-synthesized extracellular polymeric substances (EPS), constituting a dense structure known as biofilms.<sup>8</sup> The EPS matrix in biofilm serves as a firm physical barrier that restricts the penetration of antimicrobial agents,<sup>9</sup> thus making the bacteria drug-resistant and increasing the difficulty of complete wound regeneration.<sup>9</sup> The existence of biofilms severely hinders the conventional approach to the clinical treatment of infections. Therefore, it is imperative to develop alternative methods and antibiotic-free

<sup>a</sup> Guangxi Colleges and Universities Key Laboratory of Natural and Biomedical Polymer Materials, Guangxi Key Laboratory of Optical and Electronic Materials and Devices, and College of Materials Science and Engineering, Guilin University of Technology, Guilin 541004, P. R. China. E-mail: [liuchanjuan@glut.edu.cn](mailto:liuchanjuan@glut.edu.cn), [huangxiaohua@glut.edu.cn](mailto:huangxiaohua@glut.edu.cn)

<sup>b</sup> State Key Laboratory for Chemistry and Molecular Engineering of Medicinal Resources, School of Chemistry and Pharmaceutical Science, Guangxi Normal University, Guilin, 541001, China

† Electronic supplementary information (ESI) available. See DOI: <https://doi.org/10.1039/d3tb02040a>

wound dressings to combat microorganism infections, especially to eradicate the formed bacteria biofilms.

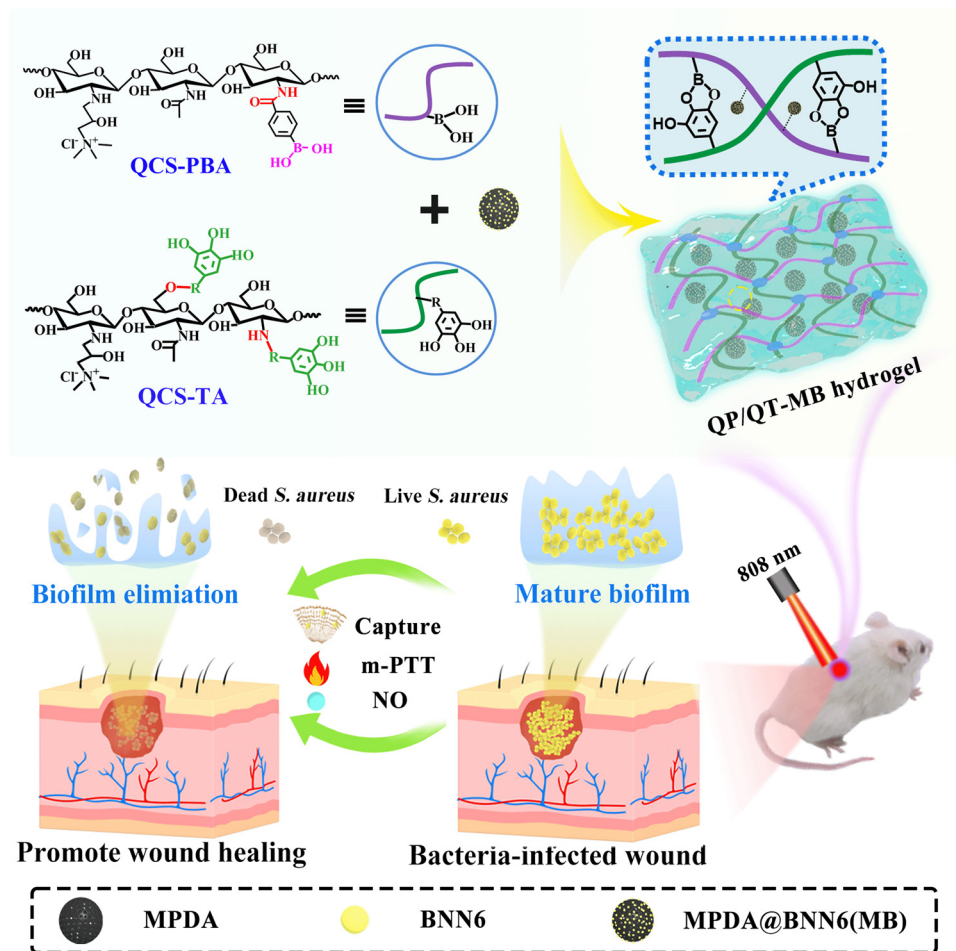
Recently, photothermal therapy (PTT) has been studied as an alternative to antibiotics to treat infected wounds with biofilms.<sup>10</sup> PTT based on near-infrared (NIR) laser-absorbing nanomaterials is capable of converting absorbed photonic energy into localized hyperthermal and then thermally ablating planktonic bacteria and biofilms by destroying the structure and components of microorganisms under NIR light irradiation, meriting the advantages of non-invasiveness, deep tissue penetration,<sup>11</sup> and circumventing drug resistance. In addition, localized NIR illumination could improve blood circulation and reduce inflammation in tissue, which are positive for wound repair. To date, various photothermal conversion materials have been exploited for photothermal inactivation of microorganisms,<sup>12</sup> including noble metal nanocomposites, carbon-based nano-platforms, metal sulfide nanomaterials, black phosphorus nanosheets,<sup>13–16</sup> and conjugated polymer-based composites.<sup>17,18</sup> Among them, melanin-like polydopamine-based photothermal agents possess good biocompatibility, high photothermal conversion performance, and facile functionalization.<sup>19,20</sup> In particular, mesoporous polydopamine (MPDA) possesses large surface-to-volume ratios and a high capacity for loading various biomolecules and therapeutic agents, and has attracted extensive interest.<sup>21,22</sup> However, the working temperatures of efficient PTT commonly require higher than 60 °C to completely eliminate bacterial populations and the photothermal agents are not capable of selectively binding the pathogenic microbe or biofilms,<sup>12</sup> which results in irreversible thermal damage to the surrounding healthy tissues.<sup>23,24</sup> Moreover, the monotherapy approach is not as effective as anticipated in the fight against biofilm infections. Therefore, these issues highlight the need for alternative systems that combine mild-temperature photothermal therapy (m-PTT, < 50 °C) with efficient targeting or combinational therapy.

Nitric oxide (NO), an endogenously gaseous molecule, that is essential for pathophysiological and physiological processes, has recently been regarded as a promising broad-spectrum antibacterial agent through disruption of the bacterial membrane, DNA, and proteins. It has been demonstrated that the NO molecule is able to deeply penetrate the biofilm and produce reactive nitrogen species for bacterial inactivation.<sup>24</sup> In particular, unlike conventional antimicrobial agents, a low concentration of NO (< 1.0 μM) also promotes wound regeneration *via* multiple mechanisms including increasing myofibroblast, collagen deposition, and wound contraction.<sup>25,26</sup> The combination of NO and m-PTT would be a desirable strategy not only to eliminate the established biofilm but also reduce the risk of localized hyperthermia.<sup>27,28</sup> Meanwhile, photothermal-mediated NO controlled release platforms have become the most compelling due to allowing precise control of NO delivery and release on demand.<sup>29,30</sup> Among various types of NO donors, *N,N'*-di-*sec*-butyl-*N,N'*-dinitroso-1,4-phenylenediamine (BNN6) is one of the Bis-*N*-nitroso compounds commonly used as NO donors, that can decompose to generate NO molecules. But the BNN6 donor molecular shows low water solubility, which impedes its practical

application.<sup>28,31</sup> The MPDA-based photothermal material possesses abundant hydroxyl and amino hydrophilic groups, and a rich porous and conjugated  $\pi$  structure, which can carry various type of hydrophobic or hydrophilic small molecules through  $\pi$ - $\pi$  stacking or physical adsorption, and has been used widely in drug delivery.<sup>21,22</sup> Consequently, integrating NIR laser-mediated photothermal component MPDA and the NO release donor BNN6 into a hydrogel system to achieve synergistic therapy effects, especially for biofilm-infected wound repair, is extremely valuable.

Injectable hydrogels are capable of *in situ* coating drugs, fitting irregular wounds and self-healing adhesive hydrogel to protect wounds from damage,<sup>32</sup> especially in the frequent movement of skin wounds.<sup>33,34</sup> Hydrogels established with reversible crosslinks, including physical interactions (*e.g.*, ionic interactions, hydrogen bonding, and host-guest interactions) and dynamic covalent linkages (*e.g.*, Schiff base reactions, borate ester bonds, and Diels-Alder reactions) enable the hydrogel network with injectability and self-healing abilities. Thus, they could seal the wound *in situ* and repair the damage autonomously.<sup>35</sup> Among them, the dynamic covalent borate ester-based injectable self-healing hydrogel dressing is more suitable for skin motion wounds, in particular, the hydrogel cross-linked with boronic acid/polyphenol exhibits an excellent tissue wet-adhesion ability through a catechol-like mimicking mussel adhesion reaction with the wound wet tissue.<sup>36</sup> More importantly, boronic acid can also act as a functional group in the esterification with polysaccharides like lipopolysaccharides and peptidoglycans on the bacterial cell wall, thus enabling targeted bacterial attachment, amplifying bacterial accumulation on the hydrogel dressing and enhancing the anti-infection effect.<sup>37,38</sup>

Quaternized chitosan (QCS), with excellent biocompatibility, water solubility, antimicrobial activity, and hemostatic ability, has become a promising candidate for wound dressing applications.<sup>39,40</sup> QCS as a hydrogel backbone imparts endogenous antimicrobial properties to the dressing, thereby increasing the antimicrobial efficiency of the hydrogel in combination with mild photothermal and NO synergistic therapies. According to all the above considerations, we present a novel multifunctional hydrogel platform (QP/QT-MB) based on dynamic boronic acid/catechol-like cross-linking between phenylboronic acid functionalized QCS (denoted as QP) and TA-modified QCS (denoted as QT) in conjunction with the *in situ* incorporation of BNN6-loaded MPDA nanoparticles (MPDA@BNN6 NPs), the prepared QP/QT-MB versatile hydrogel possessing injectable, self-healing, wet adhesiveness, intrinsic antimicrobial, and NIR laser-mediated photothermal and NO controlled release abilities for synergistically combating against as-formed bacteria biofilms and promoting infected wound healing (Scheme 1). Benefiting from the glycocalyx-mimicking phenylboronic acid on the QCS backbone with bacteria affinity facilitates planktonic bacteria to attach to the hydrogel surface, thereby leading to the increased exposure of bacteria or dissipated biofilm fragments to the inherent antimicrobial hydrogel backbone, which causes contact-damage of bacteria, thus making them sensitive to the m-PTT and NO therapy. Once exposed to NIR lasers, the synergistic mild photothermal effect



**Scheme 1** Schematic of the preparation of multifunctional QP/QT-MB hydrogel and its application in anti-infection and wound healing.

and heat-triggered NO release achieved enhanced sterilization behavior, contributing jointly to induce the dispersal of biofilms and disruption of the bacteria plasma membranes, which further caused leakage and damage of intracellular components, resulting in the inactivation of bacteria and finally eliminating biofilm. Furthermore, all the components of QCS, TA, and MPDA in the hydrogels, as well as the low concentration of NO in the absence of laser irradiation, will synchronously improve the wound micro-environment, tissue adhesion sealing, relieve inflammation and promote wound healing, which can satisfy the demands of severe infected cutaneous wounds. The versatile therapeutic hydrogel displays high efficiency in the treatment of cutaneous wound models with biofilm infections while exhibiting no distinct toxicity. The designed NO-synergistic photothermal multifunction hydrogel provides a potential strategy for treating biofilm infections and wound healing.

## Experimental section

### Synthesis of MPDA NPs

Pluronic F127 and 1,3,5-trimethylbenzene (TMB) were used as organic templates to prepare MPDA nanoparticles (MPDA NPs)

in a facile one-step synthesis.<sup>41</sup> First, Pluronic F127 (0.36 g) and TMB (415  $\mu$ L) were dissolved in a solvent mixture of water/ethanol (60/60 mL) and stirred for 30 min. Then, 60 mg of dopamine hydrochloride and 90 mg of tris(hydroxymethyl)-aminomethane (Tris) were added, and the reaction was carried out for 24 h. Finally, the MPDA NPs were obtained by centrifugation after washing three times with ethanol and acetone.

### The synthesis of BNN6 and MPDA@BNN6 NPs

BNN6 was synthesized using the following method.<sup>42</sup> In brief, *N,N'*-di-*sec*-butyl-1,4-phenylenediamine (BPA, 2.34 mL) was diluted with 20 mL ethanol, and sodium nitrite solution (6 M, 20 mL) was added and stirred for 30 min. Then HCl (6 M, 20 mL) was added slowly using a syringe and the reaction was carried out for 4 h. Finally, the prepared BNN6 was collected by centrifugation and stored away from light (Fig. S5A and C, ESI†).

For the BNN6 loading,<sup>20</sup> 2.0 mg of MPDA was suspended in 2 mL of deionized water, and then 2 mL of different concentrations of BNN6 solution (0.2, 0.4, 0.6, 0.8, 1.0, and 1.2 mg mL<sup>-1</sup> ethanol) was added and reacted for 24 h. The BNN6-loaded MPDA (denoted as MPDA@BNN6) was obtained by washing it

with deionized water. The loading capacity of BNN6 was determined by UV absorption at a wavelength of 258 nm.

### *In vitro* NO release study

The release of NO from the sample solution (MPDA@BNN6 NPs and QP/QT-MB hydrogel) was monitored using the commercial Griess assay kit. Freshly prepared samples were immersed in 1 mL phosphate buffered solution (PBS, pH = 7.4) and irradiated with or without an 808 nm NIR laser ( $1.0 \text{ W cm}^{-2}$ ), respectively. Then BNN6 was decomposed into NO and the byproduct *N,N'*-2,5-cyclohexadiene-1,4-di-*sec*-butylamine (BHA) (Fig. S5B, ESI†). To determine the concentration of released NO, the standard curve was constructed using the  $\text{NaNO}_2$  aqueous solution (10, 20, 40, 60, and 80  $\mu\text{M}$ ) (Fig. S17, ESI†). 60  $\mu\text{L}$  of the leachate was taken out at a predetermined time and incubated with Griess reagent to form diazo compounds, and the absorbance value at 540 nm was measured with a microplate reader.

### Preparation of QP/QT-MB hydrogels

Phenylboronic acid grafted QCS (QCS-PBA) was synthesized using a previously published method.<sup>43</sup> QCS (0.04 g) was dissolved in morpholine ethanesulfonic acid (MES) buffer solution, then 4-carboxyphenylboronic acid (PBA, 0.04 g), 1-ethyl-(3-dimethylaminopropyl) carbodiimide hydrochloride (EDC, 0.047 g) and *N*-hydroxysuccinimide (NHS, 0.034 g) were added and reacted for 48 h. The sample solution was dialyzed in deionized water for 8 d (MWCO 8000–14 000) and lyophilized to obtain QCS-PBA.

The synthesis of tannic acid-modified QCS (QCS-TA) is as follows.<sup>44–46</sup> 0.05 g of QCS was thoroughly dissolved in 5 mL of deionized water, followed by the addition of 0.1 mL  $\text{H}_2\text{O}_2$  ( $1 \text{ mol L}^{-1}$ ) and 0.006 g ascorbic acid and stirred for 30 min. Then, TA solution (5 mL, 5.0 wt%) was dropped into the QCS solution under ultrasonication and the reaction was carried out for 24 h. In order to remove unbonded free TA, the obtained solution was dialyzed in deionized water for 7 days (MWCO 3500) and then freeze-dried.

Afterward, the hydrogel was conveniently prepared by simply mixing the QCS-TA and QCS-PBA solutions. Briefly, the QCS-TA aqueous solution (5.0 wt%, 1 mL) was slowly added to the QCS-PBA aqueous solution (10.0 wt%, 2 mL) under ultrasonication, then the mixing solution was left at room temperature for gelling, and the gelation process was monitored using the vial inverted method, the vial containing the precursor solution was inverted for 2 minutes, and when the mixed solution in the vial no longer flowed down it was regarded as having formed a hydrogel. As a result, the homogeneous and stable hydrogel (denoted as QP/QT) was formed quickly within 60 s at room temperature. To obtain MPDA or MPDA@BNN6 loaded hydrogels, MPDA or MPDA@BNN6 NPs were mixed with QCS-TA composite in advance, respectively, and then the same gelling procedure was carried out to prepare the multifunctional hydrogels. The MPDA loaded QP/QT hydrogel was denoted as QP/QT-M, and the MPDA@BNN6 loaded QP/QT hydrogel denoted as QP/QT-MB.

### Tissue adhesion strength assessment of hydrogels

To assess the tissue adhesion strength of QP/QT, QP/QT-M, and QP/QT-MB hydrogels, lap-shear tests were performed.<sup>43</sup> The hydrogels were coated on the gap (30 mm  $\times$  10 mm) between two pieces of porcine skins with a bonding area of 20 mm  $\times$  10 mm and then placed at 25  $^\circ\text{C}$  for 2 h to make the hydrogels thoroughly adhere to the porcine skins. Finally, the adhesive strength of different hydrogels was tested on a material testing system (MTS Critaries43, MTS Critarion).

### The affinity of the hydrogel toward bacteria

The affinity of the QP/QT-MB hydrogels with bacteria was evaluated using the solution-turbidity test. Briefly, 1.0 mL of bacterial suspension at working concentration ( $\text{OD}_{600} = 1.0$ ) were co-cultured with QP/QT hydrogel, QP/QT-M hydrogel, and QP/QT-MB hydrogel (500  $\mu\text{L}$  each) for 1 h under static conditions, respectively. Then, the  $\text{OD}_{600}$  of the mixture supernatant was measured using a microplate reader (Multiskan™ FC, Thermo-Fisher, MA, USA), and Tryptone soy broth (TSB) suspension co-cultured with PBS was set as the Control. The adhesion rate of bacteria (%) =  $(\text{OD}_{\text{PBS}} - \text{OD}_{\text{hydrogel}})/\text{OD}_{\text{PBS}} \times 100\%$ . Where  $\text{OD}_{\text{hydrogel}}$  is the  $\text{OD}_{600}$  value of bacteria after treatment with hydrogels, and  $\text{OD}_{\text{PBS}}$  is the  $\text{OD}_{600}$  value after treatment with PBS.

### Evaluation of the antibacterial and antibiofilm activity *in vitro*

The plate counting method was used to investigate the antibacterial activity of the hydrogel dressings. *Escherichia coli* (*E. coli*) and *Staphylococcus aureus* (*S. aureus*) suspension (200  $\mu\text{L}$ ,  $1.0 \times 10^8 \text{ CFU mL}^{-1}$ ) was cultivated with TSB (700  $\mu\text{L}$ ) in 48-well plates at 37  $^\circ\text{C}$  for 48 h, and the TSB culture solution was then replaced with fresh TSB and the unattached bacteria were cleaned with 0.9% sodium chloride. Afterwards, 600  $\mu\text{L}$  of the QP/QT, QT/QT-M, and QP/QT-MB hydrogels were separately added into the well plates and co-incubated in a 37  $^\circ\text{C}$  shaker, followed by irradiation with or without a 808 nm NIR laser for 10 min ( $1.0 \text{ W cm}^{-1}$ ); the temperature of the hydrogel was controlled below 50  $^\circ\text{C}$  during illumination. The PBS treated group was used as the control. Subsequently, 1 mL of sterilized PBS was added to each well to resuspend the treated bacteria and the bacterial suspensions were serially diluted 1000 times with PBS. For agar plating, 100  $\mu\text{L}$  of the diluted suspensions were spread uniformly onto LB agar plates using a sterile spreader, and incubated overnight (12 h) at 37  $^\circ\text{C}$  for colony-forming unity (CFU) counting. The number of bacterial colonies in each group was counted and the anti-bacterial efficiency is calculated according to the following formula: anti-bacterial efficiency =  $(A_{\text{control}} - B_{\text{treatment}})/A_{\text{control}} \times 100\%$ . Where  $A_{\text{control}}$  is the number of colony-forming units (CFU) in the Control group (PBS), and  $B_{\text{treatment}}$  is the number of CFUs in the treatment groups.

To further investigate the antibiofilm mechanism of the hydrogel dressing, the biofilm formed by *S. aureus* was used as an experimental object to evaluate the elimination of biofilm performance of the hydrogel dressings by crystal violet staining, SEM, and 3D confocal scanning microscopy (3D CLSM).



*S. aureus* suspension ( $200\ \mu\text{L}$ ,  $1.0 \times 10^8\ \text{CFU mL}^{-1}$ ) was incubated with TSB ( $700\ \mu\text{L}$ ) in 48-well plates at  $37\ ^\circ\text{C}$ , and the medium was changed with fresh TSB every 24 h. After 48 h of co-culturation, the TSB culture solution was removed and the unattached bacteria were cleaned with 0.9% sodium chloride to obtain the biofilm attached on 48-well plates. To evaluate the anti-biofilm activity of multifunctional QP/QT-MB hydrogels *in vitro*, four groups were designed: control (PBS), QP/QT, QP/QT-M + NIR, and QP/QT-MB + NIR.  $600\ \mu\text{L}$  of the hydrogels were co-incubated with mature *S. aureus* biofilm and then irradiated with or without an 808 nm NIR laser for 10 min with a power density of  $1.0\ \text{W cm}^{-2}$ .

### Crystal violet staining

After the different treatments, the residual bacterial biofilms were stained with crystal violet (0.1%) for 10 min, and the dye was removed and washed 5 times with 0.9% sodium chloride. Then, the stained biofilms were dissolved in ethanol ( $500\ \mu\text{L}$ ,  $v/v = 95\%$ ), and the remaining biofilm biomass was evaluated by detecting the absorbance at 595 nm.

### Morphological observation of bacterial biofilms

The morphology of bacterial biofilms in the Control (PBS), QP/QT, QT/QT-M + NIR, and QP/QT-MB + NIR groups was observed using SEM. Simply, the treated biofilms were lightly cleaned with PBS (5 times) and fixed with 2.5% glutaraldehyde ( $4\ ^\circ\text{C}$ , 4 h), and then dehydrated with ethanol of different concentration gradients (30, 50, 70, 80, 90, and 100%) for 30 min each. After that, the biofilm samples were desiccated and observed by SEM *in silico*.

### Live/dead staining observation of biofilms

The bacterial biofilms subjected to different treatments including the Control (PBS), QP/QT, QT/QT-M + NIR, and QP/QT-MB + NIR were stained with fluorescence diacetate (FDA,  $100.0\ \mu\text{g mL}^{-1}$ ) and propidium iodide (PI,  $25\ \mu\text{mol L}^{-1}$ ) for 15 min in the dark. Then, sterilized slides with adhered *S. aureus* biofilm were washed with PBS solution and visualized under three-dimensional confocal laser scanning microscopy (CLSM).

### *In vivo* anti-infection and wound healing

A severely infected wound model was established to evaluate the synergistic biofilm eradication effect of the multifunctional hydrogel *in vivo*. Simply, anaesthetized mice were shaved and disinfected on the left dorsal side, and circular wounds of approximately 7.0 mm in diameter were constructed with surgical scissors and infected with  $100\ \mu\text{L}$  of *S. aureus* suspension ( $1.0 \times 10^8\ \text{CFU mL}^{-1}$ ). After 2 d of infection, the mice were set into five groups ( $n = 5$ ): control (PBS), QP/QT, QP/QT-MB, QP/QT-M + NIR, and QP/QT-MB + NIR, and the infected wounds of mice were covered with *in situ* injection  $200\ \mu\text{L}$  QP/QT, QP/QT-M, and QP/QT-MB hydrogel, respectively. The Control groups were treated with  $200\ \mu\text{L}$  PBS. Then, the infected wounds in the NIR treatment groups were illuminated with an 808 nm laser at a power density of  $1.0\ \text{W cm}^{-2}$  for 5 min.

To monitor the wound healing process, the wound locations were photographed on days 0, 2, 4, 6, and 8 post-treatment, and the wound dimensions were calculated using Image J software. After 8 days of treatment, infected skin tissues were removed for homogenization and diluted with 0.9% sodium chloride. Then,  $100\ \mu\text{L}$  of the dilution was applied for evenly coating on Luria-Bertani (LB) agar plates and cultured for 18 h for colony counting. Besides, to observe the eradication of bacterial biofilms more directly, the infected skin tissues in the wound area were obtained before and after treatments. After fixing with paraformaldehyde (4%) and gradually dehydrating using 30, 50, 70, 80, 90, and 100% ethanol solutions, the samples were sprayed gold and then observed using SEM (S4800, JEOL, Japan). The relative wound closure rate was obtained by the following formula: relative wound closure (%) =  $(S_{\text{day } 0} / S_{\text{day } n}) \times 100\%$ , where the  $S_{\text{day } 0}$  means the wound size on day 0 and the  $S_{\text{day } n}$  described the wound size on day  $n$  ( $n = 2, 4, 6$  and 8). Furthermore, post-treatment cutaneous wound tissues were collected and fixed in 4% formalin for histological evaluation by hematoxylin-eosin staining (H&E) and Masson's trichrome staining.

## Results and discussion

### Synthesis and characterization of the MPDA@BNN6 NPs

MPDA was synthesized *via* the self-polymerization of dopamine in an ammonia solution utilizing TMB and Pluronic F127 as the templates. The as-prepared MPDA displayed a spherical morphology with a diameter of approximately 150 nm (Fig. S1, ESI<sup>†</sup>), and its surface exhibited a well-defined mesoporous structure that was evenly distributed in size (Fig. 1A and B). Fig. S2 (ESI<sup>†</sup>) illustrated the  $\text{N}_2$  absorption-desorption curve of MPDA, exhibiting behavior characteristic of the mesoporous materials and matching a type-IV isotherm. The average pore size of MPDA was 5.2 nm with a Brunauer-Emmett-Teller (BET) surface area of  $20.5\ \text{m}^2\ \text{g}^{-1}$ . The large specific surface area and regularly organized pore structure of MPDA NPs contribute together to the excellent photothermal conversion efficiency ( $\eta = 30.0\%$ ) compared to that of spherical PDA nanoparticles ( $\eta = 16.6\%$ ) (Fig. S3 and S4, ESI<sup>†</sup>).<sup>47</sup>

BNN6, as a thermo-responsive NO donor, was synthesized according to the previously reported procedures (Fig. S5A-C, ESI<sup>†</sup>).<sup>42</sup> After being loaded with BNN6, the pores on the surface of MPDA@BNN6 NPs have been blurred and noticeably reduced, suggesting that BNN6 was absorbed into both the pores and the surface of MPDA NPs (Fig. 1C). Furthermore, the FTIR spectrum of MPDA@BNN6 displayed similar absorption peaks to those of BNN6 (Fig. 1D). The new absorption peaks at  $1413\ \text{cm}^{-1}$  and  $1375\ \text{cm}^{-1}$  were associated with the N-N=O and C-H stretching vibrations from the sec-butyl groups, respectively.<sup>20</sup> The characteristic peak of C-N stretching vibration was presented at  $1295\ \text{cm}^{-1}$ . The weak absorption at  $724\ \text{cm}^{-1}$  could be assigned to the bending vibration peak of C-N-N. Therefore, the above analysis indicated the successful preparation of MPDA@BNN6 NPs. Moreover, the absorption

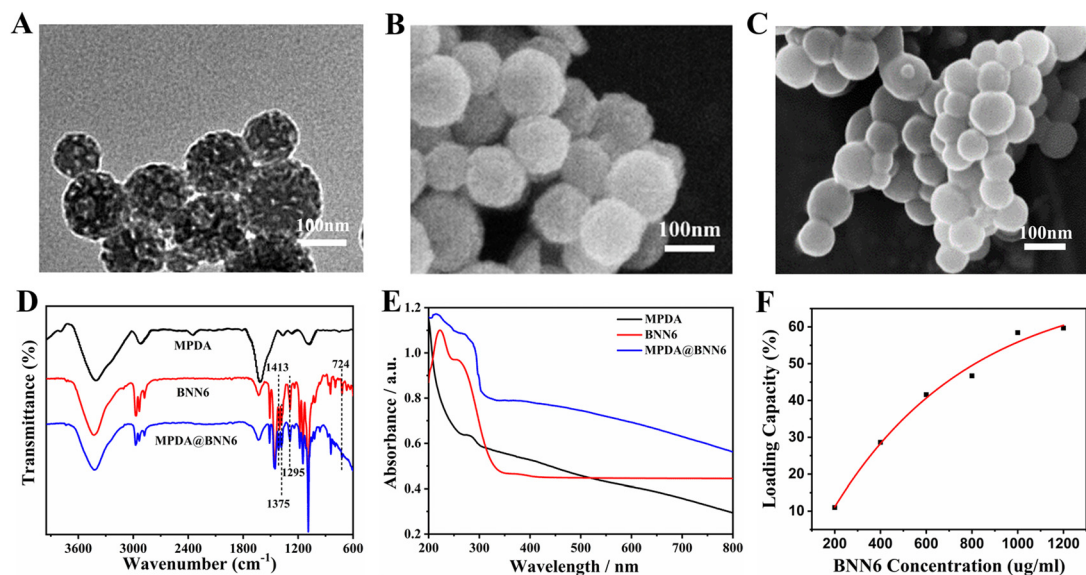


Fig. 1 (A) TEM photograph of the prepared MPDA NPs. (B) and (C) SEM photographs of the prepared MPDA NPs and MPDA@BNN6 NPs. (D) and (E) FTIR and UV-vis spectra of MPDA NPs, BNN6, and MPDA-BNN6 NPs. (F) The drug load ratio of BNN6 under different concentrations.

band at 258 nm in the UV-vis spectrum of MPDA@BNN6 also demonstrated that BNN6 has been integrated into MPDA NPs (Fig. 1E). Due to the intense  $\pi$ - $\pi$  stacking interaction between MPDA NPs and BNN6, the resultant loading efficiency of BNN6 was calculated to be as high as 58.7% based on the standard curve of BNN6, and the loading efficiency was positively correlated with the concentration of the added BNN6 (Fig. 1F and Fig. S6, ESI<sup>†</sup>).

### Preparation and characterization of QP/QT-MB hydrogels

As a cationic antimicrobial agent, QCS is a water-soluble chitosan derivative with enhanced antimicrobial activity. Positively charged quaternary ammonium groups in QCS electrostatically bind to negatively charged bacterial membranes to exert antimicrobial effects. Phenylboronic acid is considered as a glycocalyx-mimicking molecule that binds specifically to diol-containing saccharides on microorganism surfaces *via* boronic acid-diol formation.<sup>48</sup> QCS conjugated with phenylboronic acid moieties can specifically capture abundant bacteria causing contact damage of bacterial plasma membranes by QCS, thereby making them more susceptible to mild photothermal and NO therapy, and the synthetic route of QCS-PBA is shown in Fig. S7 (ESI<sup>†</sup>). Initially, QCS was synthesized by grafting glycidyltrimethylammonium chloride (GTMAC) on the chitosan chain and confirmed by FTIR spectra (Fig. S8, ESI<sup>†</sup>) and <sup>1</sup>H NMR (Fig. S9, ESI<sup>†</sup>).<sup>39,49</sup> Then, phenylboronic acid groups were grafted onto the QCS molecular chain through an amidation reaction. The FTIR spectra of QCS-PBA show the distinct B-O stretching peak overlapping with C-N vibrations at 1376  $\text{cm}^{-1}$ , which is enhanced by phenylboronic groups.<sup>50</sup> The characteristic peak at 1540  $\text{cm}^{-1}$  originated from the C=C bond in the aromatic ring of phenylboronic groups. As a result of the amide link with the phenylboronic moieties, the signal at 1650  $\text{cm}^{-1}$  associated with the amide C=O (amide I)

vibration is obviously intensified in the spectrum of QCS-PBA (Fig. 2B). Moreover, the <sup>1</sup>H NMR of QCS-PBA showed a characteristic signal around 7.3–7.7 ppm corresponding to the phenyl proton (Fig. 2A) and the UV-vis spectra showed a strong absorption band at 236 nm associated with the grafting of phenylboronic acid moieties (Fig. S10, ESI<sup>†</sup>), which further proved the successful synthesis of QCS-PBA. The degree of substitution for phenylboronic groups was calculated to be 11.0% based on the <sup>1</sup>H NMR spectra in Fig. 2A. As a kind of natural plant polyphenol, TA molecules possess abundant catechol-like moieties, which are able to form robust and reversible wet adhesion with skin tissues. TA-modified QCS was obtained *via* a free radical graft procedure induced by an ascorbic acid/hydrogen peroxide redox pair. The FTIR spectrum of QCS before and after conjugating with TA is shown in Fig. 2B. QCS exhibited typical bands at 1650 and 1561  $\text{cm}^{-1}$ , corresponding to amide I (C=O stretching) and primary amine (N-H) bending, respectively, then the characteristic peaks at 1480  $\text{cm}^{-1}$  represented the quaternary amino extension of QCS. The stretching of C<sub>3</sub>-OH and C<sub>6</sub>-OH in QCS was recognized by the peaks at 1078  $\text{cm}^{-1}$  and 1025  $\text{cm}^{-1}$ , respectively. After conjugating with TA, the characteristic absorptions of both QCS and TA were clearly observed. The peaks at 1714, 1613, and 1553  $\text{cm}^{-1}$  correspond to the aromatic ring stretching of TA, and the strong peaks at 1036, 1073, and 1155  $\text{cm}^{-1}$  were characteristic peaks of the saccharide structure of the QCS main chains. More importantly, the absorption bands of amino and C<sub>6</sub>-OH groups disappeared and weakened in the QCS-TA, demonstrating that the QCS was conjugated with TA.<sup>45</sup> The UV-vis spectra of QCS, TA, and TA grafted QCS are represented in Fig. S11 (ESI<sup>†</sup>). QCS displayed no obvious absorption peak ranging from 200 to 400 nm due to the lack of chromophore. TA exhibited two absorption bands at 215 nm and 272 nm, which should be assigned to the  $\pi$ -system of the aromatic rings.

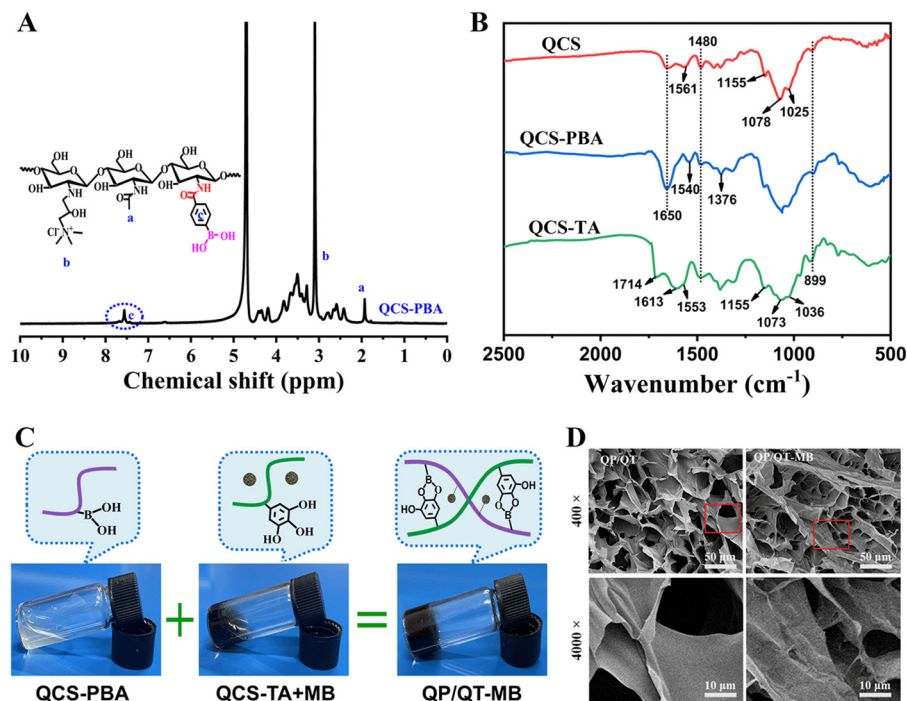


Fig. 2 (A)  $^1\text{H}$  NMR spectrum of QCS-PBA. (B) FTIR spectra of QCS, QCS-PBA, and QCS-TA. (C) The gelation process of QP/QT-MB hydrogel. (D) SEM images of QP/QT and QP/QT-MB hydrogels at different magnifications.

Similarly, QCS-TA also exhibited absorption bands of aromatic rings at 282 nm and 316 nm, confirming the insertion of TA onto QCS, the observed red shift can be attributed to the low amount of energy required for the  $n-\pi^*$  and  $\pi-\pi^*$  transition due to the covalent linkage of TA and QCS.<sup>51,52</sup> The successful grafting of TA onto QCS was also confirmed by  $^1\text{H}$  NMR spectroscopy. In the  $^1\text{H}$  NMR spectrum of QCS-TA (Fig. S12, ESI<sup>†</sup>), two characteristic peaks at 3.1 and 2.3 ppm were assigned to the protons of trimethylammonium and *N*-acetyl glucosamine units, respectively. The multiple peaks at 3.5–4.1 ppm correspond to H-3 to H-6 of the *D*-glucosamine unit of QCS. More importantly, the peak presented at 6.9–7.3 ppm belongs to the phenyl protons of TA, and these results confirmed the successful grafting of TA onto QCS. Furthermore, the TA equivalent content was estimated to be  $50.1 \pm 1.2$  mg TAE/g in QCS-TA using the Folin-Cioaltea assay (Fig. S14, ESI<sup>†</sup>). Additionally, the molecular weight of QCS before and after conjugating with TA was determined using a viscometry method.<sup>53</sup> The viscosity average molecular weight ( $M_v$ ) for QCS and QCS-TA was estimated to be 33.2 kDa and 32.6 kDa, respectively (Table S1, ESI<sup>†</sup>), which proved that the free radical conjugated reaction had negligible impact on the molecular weight of the QCS main chain.

The QP/QT hydrogel matrix could be facilely fabricated *in situ* by simply mixing QCS-PBA and QCS-TA aqueous solutions (Fig. 2C) due to the dynamic borate crosslinking between boronic acid moieties of QCS-PBA and catechol-like moieties of QCS-TA, the hydrogels formed quickly within 60 s at room temperature and the photothermal-modulated NO generator MPDA@BNN6 NPs can be integrated into the hydrogels by pre-mixing the MPDA@BNN6 solution with the QCS-TA solution in

advance, then the same gelation process was carried out to obtain the QP/QT-MB hydrogel. The gelling mechanism of QP/QT-MB hydrogels was analyzed using the FTIR spectrum (Fig. S15, ESI<sup>†</sup>). Compared to simply mixture with each component including QCS-PBA, QCS-TA, and MPDA@BNN6 (QP + QT + MB), the prepared QP/QT-MB hydrogel displayed characteristic absorption peaks of the borate ester bond at  $1370\text{ cm}^{-1}$  and  $1452\text{ cm}^{-1}$ ,<sup>43</sup> indicating that the phenylboronic acid of QCS-PBA could form a dynamic reversible borate bond with the catechol-like groups on QCS-TA. The morphological characteristics of the hydrogels were observed by SEM. As displayed in Fig. 2D, both QP/QT and QP/QT-MB hydrogels exhibited an interpenetrating porous structure, which facilitated the adsorption of wound exudates and maintained a moist environment to promote wound healing. Under 4000-fold magnification, the QP/QT hydrogel displayed a smooth surface. In contrast, the surface of the QP/QT-MB nanocomposite hydrogel was significantly rough and the network structure seemed to be denser due to the *in situ* loading of MPDA@BNN6 NPs.

In view of the satisfactory photothermal conversion performance of MPDA NPs, the photothermal effect of the QP/QT-MB hydrogel illuminated with an 808 nm laser ( $1.0\text{ W cm}^{-2}$ ) was further evaluated. As observed in the thermal images (Fig. 3A) and the photothermal heating curves (Fig. 3B), the QP/QT hydrogel displayed neglected temperature elevation within 600 s illumination. After loading MPDA NPs, the temperature of the QP/QT-M hydrogel and QP/QT-MB hydrogel was remarkably elevated to nearly  $50^\circ\text{C}$ . After five on/off cycles of laser illumination, the temperature elevation remained stable without a notable decline, demonstrating excellent photothermal



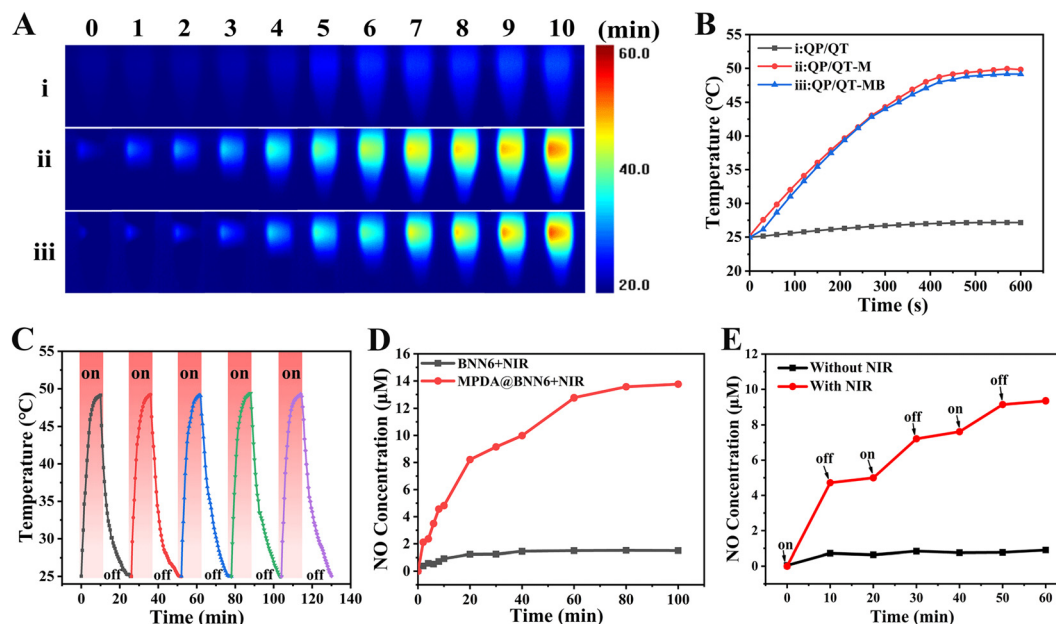


**Fig. 3** (A) Infrared thermal images of QP/QT, QP/QT-M and QP/QT-MB hydrogels illuminated with an 808 nm laser ( $1.0 \text{ W cm}^{-2}$ ). (B) Photothermal heating curves of QP/QT, QP/QT-M and QP/QT-MB hydrogels illuminated with an 808 nm laser ( $1.0 \text{ W cm}^{-2}$ ). (C) The temperature variation of the QP/QT-MB hydrogel under an on/off irradiation cycle of the 808 nm NIR laser. (D) Long-term release of NO from MPDA-BNN6 NPs ( $200 \mu\text{g mL}^{-1}$ ) and BNN6 ( $200 \mu\text{g mL}^{-1}$ ) exposure to an 808 nm laser ( $1.0 \text{ W cm}^{-2}$ ). (E) NO release from the QP/QT-MB hydrogel with or without intermittent 808 nm laser illumination ( $1.0 \text{ W cm}^{-2}$ ).

stability (Fig. 3C). The rapid increase in temperature in both hydrogels was ascribed to the MPDA-mediated superior photothermal conversion effect of the hydrogels. The photothermal heating performance of the hydrogel system relied strongly on the MPDA@BNN6 concentration, and the elevated temperature increased with increasing MPDA@BNN6 concentration. In particular, the temperature of the QP/QT-MB hydrogel increased to  $49.1^\circ\text{C}$  at the MPDA@BNN6 concentration of  $0.2 \text{ mg mL}^{-1}$  (Fig. S16, ESI†), which enabled its potential application for m-PTT ( $T < 50^\circ\text{C}$ ).<sup>48</sup> Thus, the QP/QT-MB hydrogel incorporated with  $0.2 \text{ mg mL}^{-1}$  MPDA@BNN6 was selected for subsequent investigation.

Under NIR light irradiation, MPDA-mediated localized hyperthermia can trigger thermosensitive BNN6 to produce NO effectively.<sup>13,54,55</sup> Besides, the hydrogel displayed a reversible thermos-responsive gel-sol transition at the temperature of  $48^\circ\text{C}$  due to the dynamic borate bond crosslinkage (Fig. S18, ESI†),<sup>36</sup> indicating that the mild photothermal effect can induce the gel-sol transition, thus facilitating the diffusion and release of NO gas for efficient combination therapy. As shown in Fig. 3D, when the BNN6 and MPDA@BNN6 dispersions were continuously exposed under an 808 nm laser ( $1.0 \text{ W cm}^{-2}$ ) for 100 min, significant NO ( $13.8 \mu\text{M}$ ) was released from MPDA@BNN6 NPs, whereas only a tiny quantity of NO ( $1.5 \mu\text{M}$ ) was released from the pure BNN6, indicating that the release of NO can be triggered by an MPDA-mediated photothermal effect. After loading MPDA@BNN6 NPs into the QP/QT hydrogel matrix and then illuminating intermittently at 10 minute intervals with an 808 nm laser ( $1.0 \text{ W cm}^{-2}$ ), the NO release displayed an on-demand release profile. When the NIR laser was

switched on, the massive release of NO from the QP/QT-MB hydrogel ( $4.8 \mu\text{M}$ ) was detected within the initial cycle of laser exposure for 10 min. Whereas without laser irradiation, the negligible release of NO from the QP/QT-MB hydrogel was detected ( $0.7 \mu\text{M}$ ). Once re-exposed to the laser, the NO release increased significantly again. The total amount of NO release was  $9.4 \mu\text{M}$  after three switch-on/switch-off laser exposure cycles, compared to only  $0.9 \mu\text{M}$  NO released during the 60 min without NIR exposure (Fig. 3E). Therefore, NO release from the QP/QT-MB hydrogel can be well modulated by switching the “on-off” state of the NIR laser to achieve the required treatment concentration and avoid the risk of NO poisoning.<sup>56</sup>

### Physicochemical properties of hydrogels

The injectable property of the hydrogel is valuable for wound dressings as it not only assists in minimally invasive surgery but is also appropriate for fitting irregular wounds.<sup>57</sup> As exhibited in Fig. 4A, the viscosity of the QP/QT-MB hydrogel drastically dropped when the shear rate increased from 1 to  $100 \text{ s}^{-1}$ , suggesting the shear-thinning behavior enabled the hydrogel with the potential for injectability, and the QP/QT-MB hydrogel has been proven to be easily extruded *via* a 21-G needle to form the specific letters of “China.” Given that the hydrogel is based on a dynamic cross-linked structure of borate esters, it is expected to have self-healing properties. Accordingly, the strain amplitude sweep test was further performed to investigate the self-healing properties of the hydrogel. As displayed in the continuous strain sweep curve of Fig. 4B, the storage modulus  $G'$  and storage modulus  $G''$  values were maintained at almost constant values over a strain range of 0–100%, which is



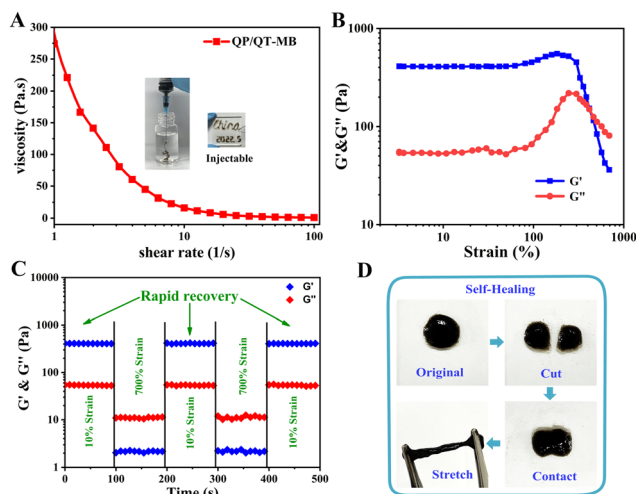


**Fig. 4** (A) The curve of shear viscosity of the QP/QT-MB hydrogel as a function of shear rate and the illustration displayed the injectability photographs. (B) Continuous strain amplitude scanning and (C) alternative step strain sweep of the QP/QT-MB hydrogel. (D) Macroscopic self-healing pictures of the QP/QT-MB hydrogel.

considered to be the linear viscoelastic region. As the strain increases, the  $G'$  and  $G''$  values decrease abruptly, and then these two values intersect at a critical strain of about 415%, suggesting hydrogel network collapse. After that, an alternate step-strain scanning test was performed by repeatedly applying a higher strain of 700% ( $>415\%$ ) and a lower strain of 10%. As illustrated in Fig. 4C, under low strains (10%), the  $G'$  value was greater than the  $G''$  value acting like an elastic solid, while changing the strain from 10% to 700%, the  $G'$  value of the QP/QT-MB hydrogel abruptly dropped below the  $G''$  value, revealing the damaged inner network and the hydrogel was liquefied. Reversely, when the shear strain decreased to the low strain of 10% again, the  $G'$  and  $G''$  rapidly returned to their original values. The collapse and repair processes of the hydrogel network could be repeated after three alternate cycles, implying the efficient self-repair ability. Additionally, we examined the macroscale self-healing capacity of the QP/QT-MB hydrogel (Fig. 4D). After splitting in half from the center of the hydrogel and having the incision interfaces in contact for a minute, the two pieces of hydrogels were healed into one integral gel again that could be stretched to almost twice its initial length, demonstrating its ultra-fast self-healing ability. Thus, the self-healing behavior of this hydrogel maintains its integrity as a wound dressing when suffering from external deformations or injuries. Furthermore, the compression strengths of QP/QT, QP/QT-M, and QP/QT-MB were determined to be 16.7, 28.4, and 26.1 kPa, respectively (Fig. S19, ESI<sup>†</sup>). All hydrogel samples did not exhibit fracture or cracking during the compression process indicating the flexibility and ductility of the hydrogel, which was attributed to the excellent energy dissipation capability of dynamic borate base networks. In comparison, the QP/QT-M and QP/QT-MB hydrogels exhibited enhanced compressive strengths, the possible reason is that the introduction of the rigid MPDA components can cause the enhancement effect of

mechanical strength through the formation of a second borate ester cross-linking network with QCS-PBA.

The adhesive capacity of the hydrogel enables the dressing to be tightly attached to the wound surface as a barrier to physically prevent wound dehydration or fluid leakage from tissue, restrain blood loss and protect the wound.<sup>58</sup> As shown in Fig. 5A, the QP/QT-MB hydrogel could firmly adhere to various substrate surfaces, including plastic, rubber, metal, glass, wood, and porcine skin. To evaluate the adhesion capability to dynamic motion skin, a sequence of external stresses is applied, including stretching, bending and twisting. The hydrogel remained tightly attached to the porcine skin without any dissociation, demonstrating the strong adhesion capability and desirable skin adaptability. Notably, the adherent hydrogel can be resistant against rinsing with water, and it remains tightly adhered to the pigskin without falling off, revealing that hydrogels have the ability to adhere to wet wound tissue. Furthermore, the porcine skin shear lap experiment was utilized to quantitatively assess the adhesion strength (Fig. 5B and Fig. S20, ESI<sup>†</sup>). The adhesive strengths of QP/QT, QP/QT-M and QP/QT-MB hydrogels were determined to be 35 kPa, 43 kPa and 40 kPa, respectively, which was substantially more significant than that of the fibrin glue (BeiXiu<sup>™</sup>, 14 kPa),<sup>59</sup> and these values were also relatively high in the recently reported chitosan-based hydrogels (Table S2, ESI<sup>†</sup>), indicating the potential of the hydrogels as a tissue adhesive or sealant in wound closure and healing. The strong adhesive properties of hydrogels are mainly attributed to the abundant catechol-like polyphenol moieties on QCS-TA and MPDA, which are similar to the key component in adhesive mussel foot proteins. The substantial catechol-like groups inside the hydrogel have the ability to form different types of covalent or/and noncovalent reactions with skin tissues,<sup>60–62</sup> including hydrogen bonds, Michael addition, and  $\pi$ - $\pi$ /cation- $\pi$  interactions, which enabled the excellent interfacial adhesion (Fig. S21, ESI<sup>†</sup>). Meanwhile, it is reported that the positive  $R_3NH^+$  groups in the QCS of the hydrogel could disturb the hydrated isolate layer, displace hydrated cations on the tissue surface, enhance the catechol-like moieties to access the nucleophiles (e.g., amines, thiols, and amide bonds) on the wet tissue, and cause the robust wet adhesion desired for the wound microenvironment.<sup>48</sup> Moreover, the adhesion strength of the hydrogels depends on both the interfacial adhesiveness and the cohesion of hydrogels. Compared to QP/QT, the QP/QT-M and QP/QT-MB hydrogel possessed an improved tissue adhesion ability, which should be attributed to the introduction of MPDA NPs, that not only increased the catechol moieties, but could also form a second borate ester-based cross-linked network with the hydrogel backbone (QCS-PBA), resulting in enhanced cohesive forces and interfacial adhesion. In addition, the WVTR of the QP/QT-MB hydrogel dressing was determined to be  $2191.1 \text{ g m}^{-2} \text{ day}^{-1}$  with respect to the non-covering blank control ( $4517.9 \text{ g m}^{-2} \text{ day}^{-1}$ , simulate as an open wound), excess evaporation from the wound may lead to wound dehydration in an open wound, and intermediate WVTR for the QP/QT-MB hydrogel will help to maintain a moist wound healing environment

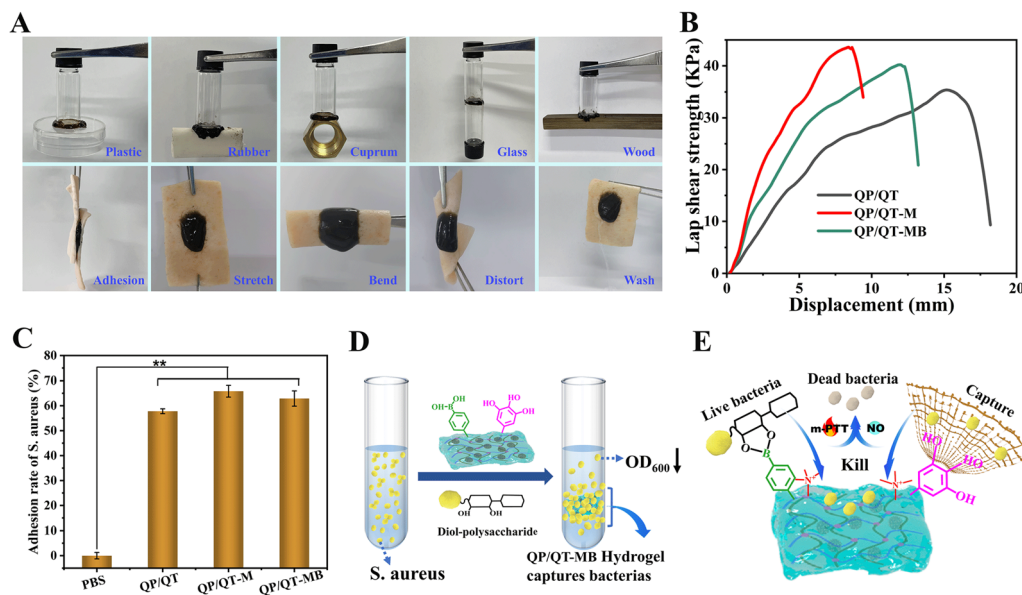


**Fig. 5** (A) Photographs of the adhesion situations of QP/QT-MB hydrogels for plastic, rubber, metal, glass, wood, and pigskin. (B) Typical force-displacement curve of the QP/QT, QP/QT-M, and QP/QT-MB hydrogels on pig skin. (C) The adhesion rate of hydrogels (QP/QT, QP/QT-M, and QP/QT-MB) for *S. aureus*. (D) Schematic representation of the adhesion of the QP/QT-MB hydrogel to bacteria. (E) Antimicrobial mechanism diagram of QP/QT-MB hydrogels: bacterial capture, intrinsic antimicrobial activity, and m-PTT/NO synergism.

(Fig. S22, ESI†).<sup>63,64</sup> Bacterial cell walls and biofilm matrices contain a large number of polysaccharides,<sup>65</sup> which have the ability to be covalently bound with phenylboronic acid to form cyclic borate esters.<sup>66</sup> Meanwhile, the cell-affinity catechol-like groups facilitate bacterial cells to attach to the hydrogel surface. Therefore, we hypothesized that the QP/QT-MB hydrogel should be able to specifically bind to bacteria. To confirm our hypothesis, the bacterial binding capacity of the QP/QT-MB hydrogel was investigated using a turbidity method (Fig. 5C and D). Briefly, the hydrogels were co-incubated with *S. aureus* for 1.0 h and the adhesion rate of the hydrogel to bacteria was calculated by detecting the OD<sub>600</sub> value of the supernatant. Compared to the PBS group, the adhesion rate of all the hydrogel groups including QP/QT, QP/QT-M, and QP/QT-MB were significantly increased to 57.2%, 66.6% and 62.8%, respectively, which indicated that the hydrogel attached with the majority of the planktonic bacteria. The specific bacterial trapping capability facilitates the disruption of bacteria plasma membranes by contact-damaging the intrinsic antimicrobial components of the positive QCS in the hydrogel dressing, thus making them sensitive to m-PTT and NO treatment (Fig. 5E).

Recent studies have demonstrated that polyphenols-modified hydrogels behave with an antioxidative ability to regulate excessive reactive oxygen species (ROS) from wounds and promote wound healing.<sup>67</sup> Consequently, the antioxidant capacity of the hydrogel was assessed by testing the scavenging efficiency for 2,2-biphenyl-1-picrylhydrazyl (DPPH) radicals. As shown in Fig. S23 (ESI†), QP/QT hydrogels and QP/QT-MB hydrogels displayed a strong DPPH scavenging efficiency with radical scavenging ratios of 85.9% and 94.2%, respectively. The QP/QT-MB hydrogels exhibited a more impressive scavenging ability than that of QP/QT hydrogels, demonstrating the

improved antioxidant activity brought about by incorporating MPDA@BNN6 NPs. According to the findings, the QP/QT-MB hydrogel dressings exhibit a promising antioxidant activity to tackle the overproduced ROS infected wounds. Moreover, the swelling performance of the prepared hydrogels was investigated by determining the water absorption capability *via* soaking the as-prepared hydrogels in PBS solution (pH = 7.4) at 37 °C. The ultimate results in Fig. S24 (ESI†) revealed all hydrogels (QP/QT, QP/QT-M, and QP/QT-MB) possessed satisfactory absorption (169.0%, 147.7% and 146.3%) after 24 h incubation, which facilitated the absorption of wound surplus exudates and maintained a moist microenvironment, preventing the loss of tissue fluid while avoiding dehydration of the wounds, thereby promoting wound healing.

### Synergistic anti-biofilm effect of QP/QT-MB hydrogels *in vitro*

Given the favorable bacterial capture ability, excellent photo-thermal effect and the precise NIR laser-controlled NO delivery property of the QP/QT-MB hydrogel, the synergistic anti-bacterial activity *in vitro* was further assessed by co-incubating with Gram-negative *E. coli* and Gram-positive *S. aureus* and then treated with or without NIR irradiation. The anti-bacterial activity was assessed using a plate counting method. It can be observed from Fig. 6A and C that the efficacies of different antibacterial strategies have similar trends for *E. coli* and *S. aureus*. There were a large number of bacteria colonies in both the Control groups (PBS) of *E. coli* and *S. aureus* with or without NIR irradiation, revealing that NIR alone does not inhibit pathogenic bacterial growth. Compared to the Control group, the bacterial survival rate in the QP/QT group revealed a certain degree of decrease due to the endogenous antimicrobial ability of QCS and TA in the hydrogel backbone,<sup>59</sup> with anti-bacterial efficiencies of

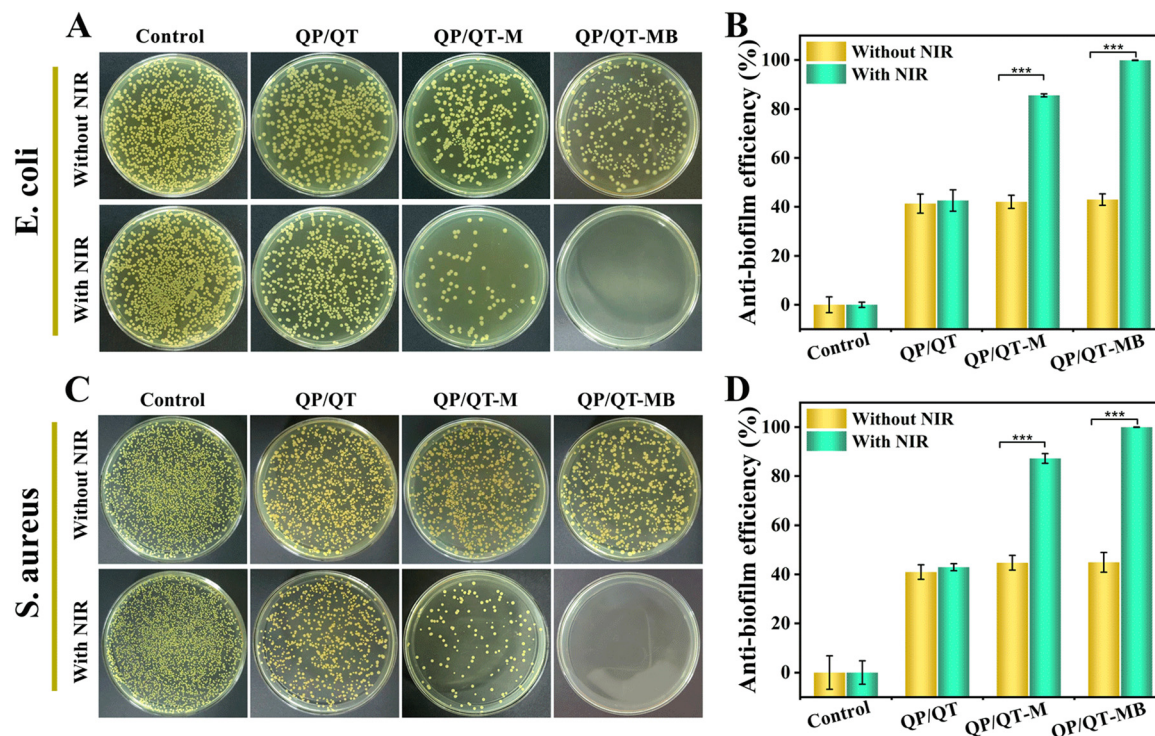


Fig. 6 (A) and (C) Representative photographs of colonies formed for *E. coli* and *S. aureus* derived from the different treated groups. (B) and (D) The corresponding statistical results of antibacterial efficiency against *E. coli* and *S. aureus* ( $n = 3$ ). \*\*\* $p < 0.001$ .

41.3% for *E. coli* and 41.0% for *S. aureus*, respectively (Fig. 6B and D). The QP/QT + NIR groups displayed similar anti-bacterial efficiencies against *E. coli* and *S. aureus* to those of QP/QT groups due to the lack of photothermal effect of the QP/QT hydrogel matrix. Moreover, after loading with MPDA or MPDA@BNN6, the anti-bacterial efficiencies of QP/QT-M and QP/QT-MB in the absence of NIR irradiation was still comparable to those of the original QP/QT hydrogel matrix, suggesting the addition of the photothermal agents or NO donor had a negligible effect on the anti-bacterial activity. Notably, the hydrogel loading with MPDA and following treatment with NIR irradiation (QP/QT-M + NIR group) exhibited a significantly increased anti-bacterial efficiency of 85.6% for *E. coli* and 87.2% for *S. aureus*, respectively, which was attributed to the MPDA-mediated mild photothermal effect enhanced by endogenous antimicrobial sensitization. More importantly, the most significant anti-bacterial efficiency was observed in the QP/QT-MB + NIR group, with anti-bacterial efficiencies up to 99.8% against *E. coli* and 99.9% against *S. aureus*, respectively, demonstrating the combination of specific bacterial capture, inherent contact-antimicrobial activity, NIR-induced mild photothermal and heat-triggered NO release can completely eliminate *E. coli* and *S. aureus*.

Pathogenic bacteria tend to cluster into biofilms with sticky multicellular communities in the wound bed. *S. aureus* is one of the bacterial colonies that is most likely to form bacterial biofilms and is commonly found in infected wounds. *S. aureus* was used as a model organism to evaluate the eliminate biofilm performance of the hydrogel dressings. Specifically, the pre-formed *S. aureus* biofilms were co-incubated with different

hydrogel dressings for 2 h and treated with or without 808 nm laser illumination, afterwards, crystal violet staining was performed to evaluate residual biofilm biomass under different treatments. As shown in Fig. 7A, the biofilms in the Control group with or without NIR treatment were dark purple, indicating the formation of dense biofilm. In contrast, only a very light pale purple was visible and the biofilm was nearly entirely eradicated in the QP/QT-MB + NIR group, demonstrating the most efficient *S. aureus* biofilm dispersal ability. According to the corresponding absorbance at the OD<sub>595</sub> value (Fig. 7B), the biofilm dissipation rate of the QP/QT-MB + NIR group was up to 96.4% compared to the Control group.

The bacterial morphologies of the biofilms before and after treatments with different hydrogel dressings were observed by SEM. As displayed in Fig. 7C, the biofilm treated with PBS (Control group) presented a smooth surface and intact plasma membranes. In contrast, some of the *S. aureus* showed a certain degree of wrinkling and deformation after treatment with the QP/QT hydrogel, which should be ascribed to the electrostatic disruption of the anionic bacteria plasma membrane by cationic QCS. Moreover, after loading MPDA into the hydrogel following irradiation with an NIR laser (QP/QT-M + NIR group), the *S. aureus* in the biofilm was seriously shriveled and collapsed, and the significantly enhanced bactericidal effect was ascribed to the localized hyperthermia mediated by MPDA. Prominently, the bacteria cell membrane presented the most severe destruction and complete fusion in the QP/QT-MB + NIR group, demonstrating the prominent biofilm elimination effect. Typically, a matured biofilm primarily comprises inner



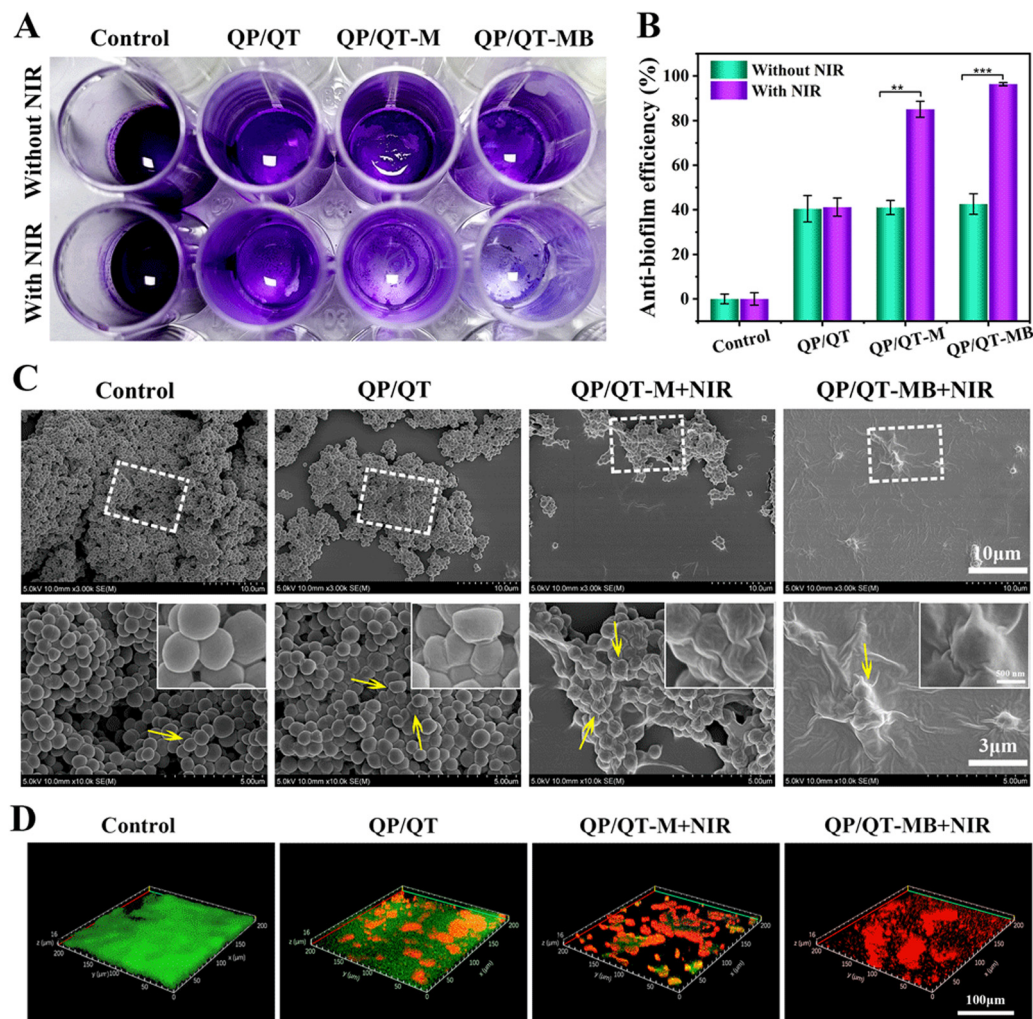


Fig. 7 (A) Pictures of crystal violet-stained biofilms and (B) quantitative analysis of anti-biofilm efficiency after different treatments. ( $n = 3$ ).  $**p < 0.01$ ,  $***p < 0.001$ . (C) SEM images of biofilms after different treatments. (D) Live/dead staining images of biofilm after being subjected to various treatments photographed by three-dimensional CLSM.

bacteria, extra-cellular polysaccharides, extra-cellular proteins, and DNA (eDNA).<sup>68–70</sup> Based on the inherent antimicrobial activity of the hydrogel matrix, conjugated with the synergistic effect of mild photothermal and NO release, the bacterial biofilm structure was entirely disrupted and the biofilm was eradicated.

Furthermore, the synergistic antibiofilm capacity was confirmed by live/dead staining. The fluorescein diacetate/propidium iodide (FDA/PI) dual-fluorescence labeling of the treated biofilm and imaging with CLSM was carried out. In this assay, PI is a red fluorescence dye that cannot pass through intact cell membranes and is used for staining only dead bacteria with damaged membranes.<sup>71</sup> FDA could be decomposed by lipases and produce fluorescein, thereby viable and intact cells produce green fluorescence.<sup>72,73</sup> As illuminated in Fig. 7D, all of the bacteria in the untreated Control group showed strong green fluorescence and displayed a dense and intact biofilm with a thickness of about 16  $\mu\text{m}$ . In contrast, a certain amount of red fluorescent signals were observed in the QP/QT treatment group and the biofilm thickness was similar to that of the

control group, suggesting that the QT/QP hydrogel disrupted the bacterial plasma membrane. Moreover, the biofilm treated with QP/QT-M + NIR showed plenty of bright red fluorescence signal and the biofilm thickness and density were dramatically decreased relative to the QP/QT group, indicating that the mild photothermal effect combined with endogenous antimicrobial activity caused severe membrane damage toward *S. aureus* in the biofilm and effectively dissipated the biofilm. Remarkably, after being treated with QP/QT-MB + NIR, almost all the *S. aureus* in the biofilm appeared as red fluorescence, demonstrating that the *S. aureus* biofilm was completely eradicated. This result was consistent with SEM and crystal violet observations. This outstanding biofilm eradication efficiency of the QP/QT-MB hydrogel was derived from bacterial capture, intrinsic antibacterial properties, and m-PTT/NO synergism.

#### In vitro biocompatibility and hemostasis

The favorable biocompatibility is a necessary prerequisite for *in vivo* biomedical applications of hydrogel dressings. The



hemolysis test was used to assess the hemocompatibility of the prepared hydrogel, and the results showed that the hemolysis rate of all hydrogels including QP/QT, QP/QT-M, and QP/QT-MB, was less than 5% within the safety limits of ISO/TR 740654 for biomaterial-related hemolysis,<sup>74</sup> confirming their excellent hemocompatibility (Fig. 8A). The cellular biocompatibility of the prepared hydrogel dressings was further assessed using a standard MTT assay and live/dead staining,<sup>75</sup> the different concentrations of QP/QT, QP/QT-M, and QP/QT-MB hydrogel leaching co-incubated with L929 cells for 12 h, and the results of the MTT test are illustrated in Fig. 8B. The cell survival rates of all the hydrogel groups were >90%, even at a relatively high concentration of 2 mg mL<sup>-1</sup>. Moreover, according to the corresponding live/dead staining assay (Fig. 8C), all of the stained cells in three hydrogel treated groups (at a concentration of 2 mg mL<sup>-1</sup>) displayed normal morphology similar to that of the control group and emitted green fluorescence (representing live cells), which demonstrates the excellent cytocompatibility of the hydrogel dressings. The above results demonstrate that the QP/QT-MB hydrogel has good biocompatibility and meets the requirements of wound management dressings, which can be further used for *in vivo* applications.

In the initial phase of wound healing, the promptness of hemostasis is critically valuable. Therefore, the hemostatic efficiencies of the hydrogel dressing *in vivo* were investigated by measuring the hemostasis time and bleeding loss in mouse liver-incision and tail-amputation models.<sup>76</sup> Commercially available medical gauze (Taizhou Xinkang Medical Materials Co., Ltd, Jiangsu, China) and gelatin sponge (Xiang'en Medical Technology Development Co., Ltd, Jiangxi, China) were used as the control groups, and a non-treatment group as the blank. As displayed in Fig. 8D for the liver trauma models, the blood loss (157.9 mg) in the blank group was obviously higher than those in the treatment groups, and the gauze reduced blood loss to 131.5 mg compared with the blank group. Whereas the gelatin sponge and hydrogel groups showed less blood loss than the blank and gauze groups, and the QP/QT-MB hydrogel exhibited the lowest blood loss of 55.4 mg. Besides, the hemostatic times of the QP/QT-MB hydrogel (64 s) and gelatin sponge group (76 s) were significantly shorter than those of the blank (110 s) and gauze groups (102 s), whereas the QP/QT-MB hydrogel group had the shortest hemostatic time (Fig. 8F). In addition, a similar trend was found in the mouse-tail amputation model (Fig. 8G), and the QP/QT-MB hydrogel and gelatin sponge still displayed a better hemostatic ability than

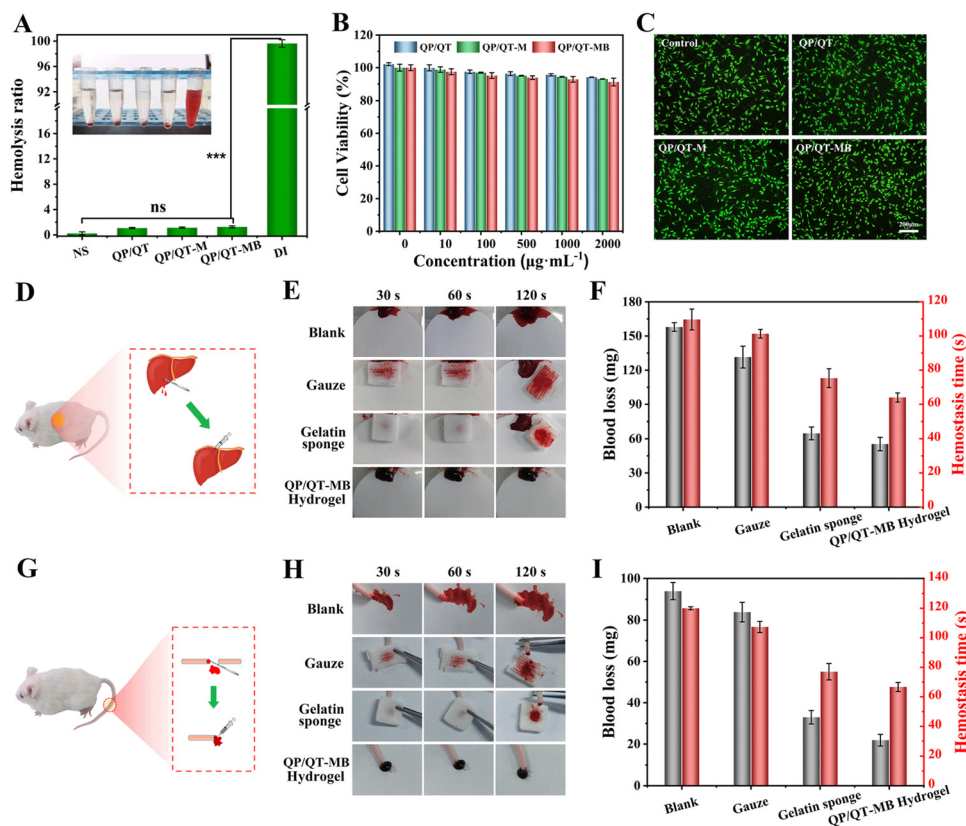


**Fig. 8** (A) Hemolysis photographs and hemolysis ratio (%) of the QP/QT, QP/QT-M, and QP/QT-MB hydrogels. \*\*\* $p < 0.001$ , ns: no significance. (B) The relative survival rate of L929 cells after co-incubating with different concentrations of QP/QT, QP/QT-M, and QP/QT-MB hydrogel leaching for 12 h and (C) the corresponding FDA/PI co-stained fluorescent images (at a concentration of 2 mg mL<sup>-1</sup>). (D) and (E) Schematic diagram and the blood stain photos of the mouse liver-incision model. (F) Blood loss and hemostatic time in the mouse liver injury model. (G) and (H) Schematic diagram and the blood stain photos of the mouse tail-amputation model. (I) Blood loss and hemostatic time in the mouse-tail amputation model ( $n = 3$ ).

the blank and gauze groups. Among all the groups, the QP/QT-MB hydrogel still presented the lowest amount of bleeding (21.9 mg) and shortest hemostatic time (67 s) (Fig. 8I). Moreover, the bloodstain photographs (Fig. 8E and H) for each group were consistent with the above quantitative results. The excellent hemostatic performance of the QP/QT-MB hydrogel might be ascribed to the synergistic effect of rapid wound sealing and clotting formation. The wet-adhesion ability of the hydrogel allows it to adhere tightly to wound tissues, serving as a barrier to physically block the hemorrhage site.<sup>77,78</sup> Meanwhile, the numerous positive amino groups and quaternary ammonium groups of QCS can adsorb negatively charged platelets to clump red blood cells and hasten thrombus formation.<sup>79,80</sup> Besides, TA has a positive hemostatic capacity due to its ability to interact with plasma proteins and the vasoconstriction effect.<sup>81</sup> The above mechanisms synchronized action to accelerate the hemostatic process.

### *In vivo* anti-biofilm and wound healing performance

Given the remarkable anti-biofilm outcomes of QP/QT-MB hydrogel *in vitro*, we further explored the antimicrobial and wound-healing performance of this multifunctional hydrogel

platform *in vivo*. The full course of the treatment scheme is displayed in Fig. 9A, and the full-thickness skin wounds (with a diameter of about 7.0 mm) were established and inoculated with *S. aureus* suspensions ( $100\ \mu\text{L}$ ,  $10^8\ \text{CFU mL}^{-1}$ ) for 2 days. Serious exudates and abscesses were visible in the wound sites, implying the successful modeling.<sup>82</sup> Subsequently, the infected mice wounds were treated by injecting a coating with different hydrogel dressings including QP/QT, QP/QT-M, and QP/QT-MB. The injected hydrogel dressing could perfectly adapt with the wound and adhere to the tissues (Fig. S25 and Video S1, ESI†). After that, the wounds were treated with or without NIR irradiation, and during the NIR-irradiation process, the temperature in the wound region was monitored by an IR camera. As presented in Fig. 9B, after 808 nm laser irradiation for 5 min, the localized temperature in the infected wound site elevated to  $48.8\ ^\circ\text{C}$  in the QP/QT-MB + NIR group, indicating the desirable m-PTT therapeutic effect of the QP/QT-MB hydrogel dressing *in vivo*, and the mild photothermal effect could not only accelerate wound regeneration but also promote NO release, thus resulting in an m-PTT/NO synergic enhanced antibacterial effect. The wounds were photographed every two days to track the wound size changes for evaluating the therapeutic effect of

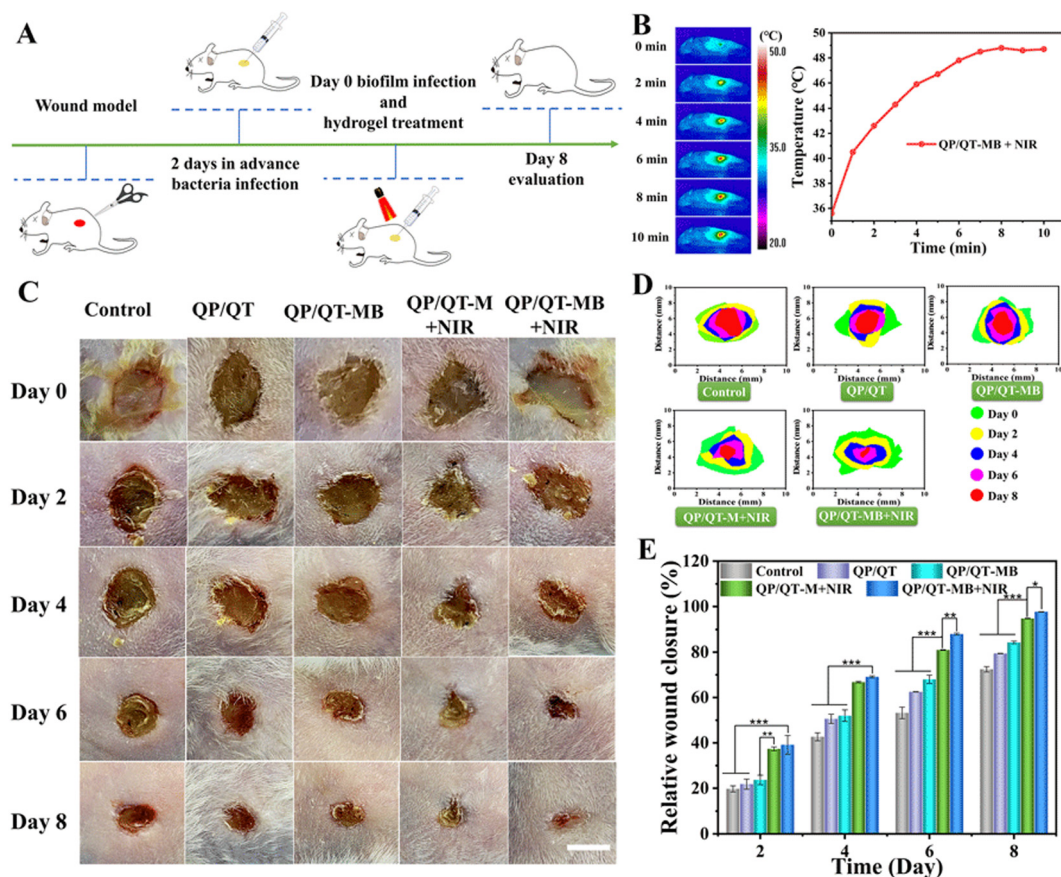


Fig. 9 (A) Schematic diagram of severely infected cutaneous wound model formation and treatment with QP/QT-MB hydrogel dressing. (B) Thermographic images and the corresponding temperature elevation curves in the wound site under the QP/QT-MB + NIR treatment group. (C) Representative images of biofilm-infected cutaneous wounds under different treatments on days 0, 2, 4, 6, and 8. Scale bar is 5 mm. (D) and (E) Schematic diagram and quantification of the changes in the wound-bed area during 8 days of treatment for each group ( $n = 5$ ). \* $p < 0.05$ , \*\* $p < 0.01$ , \*\*\* $p < 0.001$ .

each group. As illustrated in Fig. 9C–E, the wound area progressively reduced over time in all five treatment groups, and the wound size in the PBS-treated group (Control) was 72.5% of the original wound size after 8 days of treatment. In the QP/QT and QP/QT-MB treatment groups, the wound size decreased to 79.4% and 84.3%, respectively, which was mainly ascribed to the intrinsic antibacterial activity of the hydrogel matrix, whereas the slightly higher wound healing ratio in the QP/QT-MB group was supposed to be the healing-promoting effect of the sustained low concentration release of NO in the absence of NIR irradiation. In comparison, the QP/QT-M + NIR treatment group exhibited a relatively high wound closure ratio (>90.0%) due to introducing the mild photothermal-therapeutic effect, which coordinately eliminated bacteria with the inherent antimicrobial ingredients to further promote wound healing. Notably, among the five groups, the QP/QT-MB + NIR group revealed the most efficient recovery with a wound closure ratio of 97.7%, and the wound basically healed after 8 days of treatment. This was primarily due to the multi-function of the hydrogel containing m-PTT, controlled-release NO, and inherent antimicrobial activity, thereby directly eradicating bacterial biofilm infection, providing a perfect micro-environment for wound regeneration. In addition, negligible body weight changes in all the treated groups, suggested the biosafety of the hydrogel dressing (Fig. S26, ESI<sup>†</sup>). At day eight post-treatment, the wound tissues from each treatment group were collected, homogenized, and then spread on agar plates, and the persistence of bacteria under each treatment was then assessed by counting bacterial colonies. The results are shown in Fig. 10A, and as expected, only a few *S. aureus* colonies were visualized in the QP/QT-MB + NIR group, where 97.6% bacteria were removed from the infected cutaneous wound relative to the Control group after 8 days of treatments (Fig. 10B). Furthermore, the skin tissues in the wound area before and after hydrogel dressing treatment were obtained by SEM. As illuminated in Fig. S27 (ESI<sup>†</sup>), the wound tissue before treating with hydrogel dressings presented a dense and irregular biofilm structure with numerous bacterial pathogens and an EPS matrix. While the wound tissue after treating with hydrogel dressing (QP/QT-MB) and the subsequent irradiation with NIR laser displayed nearly no biofilm residue, and the bacterial morphology was severely damaged. The results proved that the QP/QT-MB hydrogel combination with 808 nm irradiation could eradicate biofilms and subsequently accelerate the process of wound healing *in vivo*.

Histological analysis was performed to further assess the wound healing status by H&E staining, Masson trichrome staining and the immunohistochemical staining of CD31 at day 8 post-treatment. Fig. 11A exhibited the pathological changes in the cutaneous wound tissues for each group. The wound was unclosed and presented severe inflammatory cell infiltration in the PBS treatment group. In contrast, the number of inflammatory cells decreased to some degree, and a thickened and inhomogeneous epidermis layer was presented in the QP/QT and QP/QT-M group, which could be ascribed to the inherent antibacterial activity of the hydrogel matrix as well as

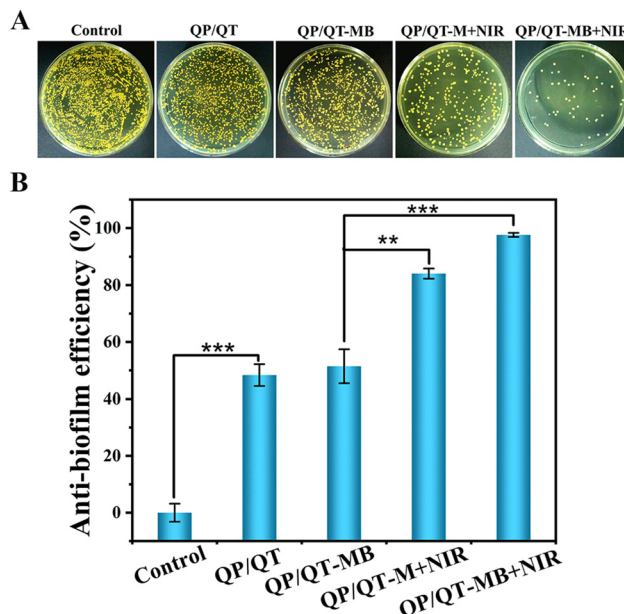


Fig. 10 (A) Pictures of agar plates of *S. aureus* collected from biofilm-infected skin wounds. (B) Statistical data of anti-biofilm efficiency for the different treatment groups *in vivo*.  $n = 5$ ,  $**p < 0.01$ ,  $***p < 0.001$ .

the anti-inflammatory effect of TA that can relieve the inflammatory response. For note, some amount of neovascularization and collagen fiber were clearly found in the wound defect area under QP/QT-MB treatment, which verified that low concentrations of NO release ( $< 1 \mu\text{M}$ ) from the nanocomposite hydrogel are beneficial to wound healing in the absence of NIR irradiation. Whereas in the QP/QT-M + NIR group, the inflammatory infiltrate was remarkably abrogated, an intact homogeneous epidermis layer and new dermis appendages, such as hair follicles and sebaceous glands, appeared in the wound tissue, which verified the mild photothermal effect induced the synergistic enhanced antimicrobial activity and promoted wound healing. Among them, the QP/QT-MB + NIR treatment group revealed the best wound-healing effect with negligible inflammatory infiltrate, almost complete regeneration of epidermis and dermal tissues, and the maximum amount of skin appendages, which was primarily ascribed to the triple wound-healing effects of m-PTT, NO release, and intrinsic antimicrobial activity.

In addition, collagen is the primary constituent of the extracellular matrix, which is essential for the healing of wounds. The result of Masson's trichrome staining (Fig. 11B) was consistent with H&E staining. The situation of collagen deposition in both the QP/QT-M + NIR and QP/QT-MB + NIR group displayed substantial collagen fibers with dense and organized distribution, in contrast to the other treatment groups, which exhibited few collagen fibers with loosely packed structures. Prominently, the dermal tissues with the distinct thickest and highest density of collagen deposition appeared in the QP/QT-MB + NIR treatment group. Moreover, the CD31 expression in the wounds treated with QP/QT-MB + NIR showed grossly more than QP/QT-MB and QP/QT-M + NIR groups,



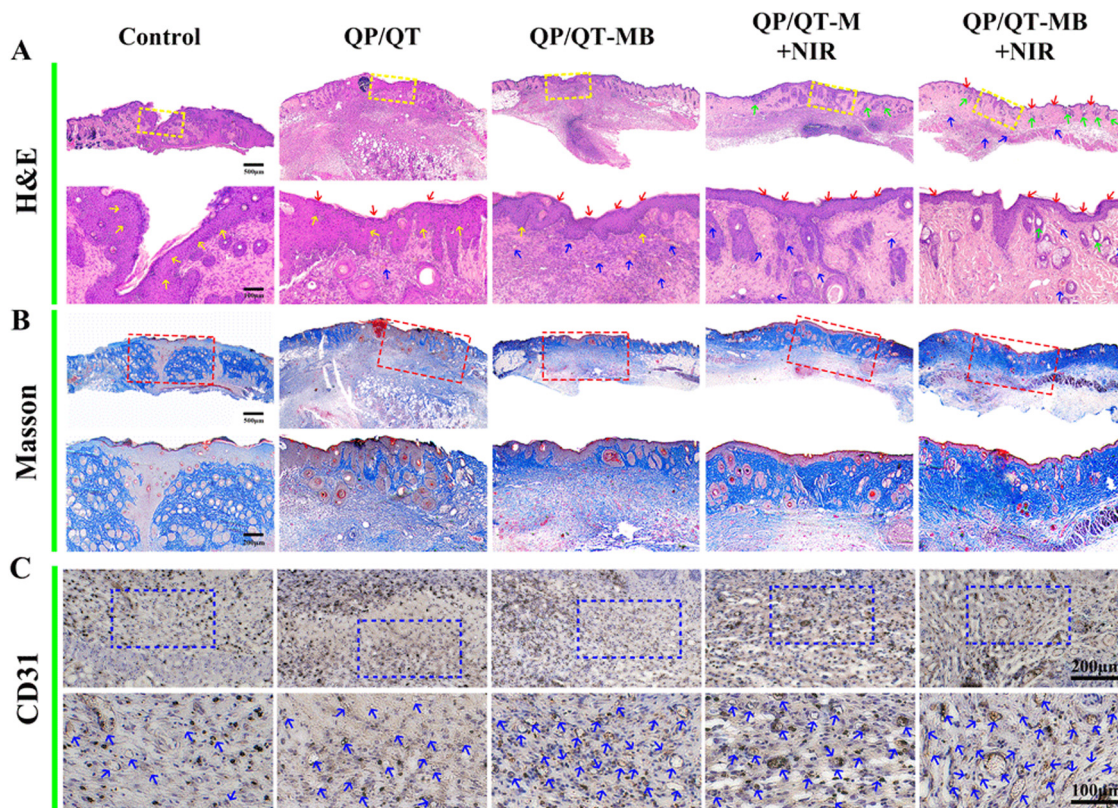


Fig. 11 (A) H&E stained, (B) Masson trichrome stained, and (C) CD31 immunohistochemical staining images of biofilm infected skin tissue after different treatments. Yellow arrow: inflammatory cells; red arrow: neonatal epidermis; green arrow: hair follicle and sebaceous glands; Blue arrow: neovascularization.

followed by QP/QT- and PBS-treated wounds (Fig. 11C and Fig. S28, ESI†). Additionally, blood vessels in the QP/QT-MB + NIR group exhibited bigger size with a lumen structure, suggesting the significant promotion of angiogenesis *via* m-PTT combined with NO release. Thus, these results clearly indicated that the QP/QT-MB hydrogel improved wound healing by eradicating biofilm infection, reducing the inflammatory response, and promoting collagen remodeling and capillaries reconstruction. Taken together, the multifunctional QP/QT-MB hydrogel combined with NIR irradiation significantly promotes the healing of biofilm-infected wounds by efficiently eliminating bacterial infection, abrogating inflammatory infiltration, accelerating epithelial cell and dermis tissue regeneration, as well as promoting collagen remodeling, verifying its enormous potential for treating severely infected biofilm wounds.

## Conclusions

In conclusion, we successfully constructed a versatile hydrogel dressing (QP/QT-MB) by dynamic crosslinking phenylboronic acid-functionalized QCS and TA-modified QCS incorporated with photothermal NO generator MPDA@BNN6. The prepared QP/QT-MB hydrogels possess facilitating injectability, desirable self-healing performance, strong tissue wet-adhesiveness, and excellent biocompatibility. Taking advantage of MPDA's

promising photothermal conversion performance and high drug loading capability for BNN6, in conjugation with the specific bacteria-capturing ability and the endogenous bactericidal activity of the hydrogel matrix, the NIR-activated QP/QT-MB hydrogel induced a combination of mild photothermal effect and controlled release of NO gas to achieve a synergetic anti-biofilm effect both *in vitro* and *in vivo*. The results of the biofilm-infection wound model experiments revealed that the multifunctional QP/QT-MB hydrogel combined with 808 nm NIR irradiation could remarkably accelerate wound healing by effectively eliminating biofilm, suppressing the inflammatory response, and improving angiogenesis and collagen deposition. In summary, this versatile hydrogel offers a promising candidate for clinical biofilm-associated infected wound management.

## Conflicts of interest

The authors declare that they have no known competing financial interests or personal relationships that could have appeared to influence the work reported in this paper.

## Acknowledgements

The authors gratefully acknowledge the financial support from the National Natural Science Foundation of China (52003064),



Guangxi Natural Science Foundation (2021GXNSFAA075016), Project of the Department of Science and Technology of Guilin (2020010906), the opening fund of Key Laboratory of New Processing Technology for Nonferrous Metal & Materials, the Ministry of Education/Guangxi Key Laboratory of Optical and Electronic Materials and Devices (No. 22KF-8), and the Doctoral Fund Project of Guilin University of Technology (GUTQDJJ6612039).

## Notes and references

- 1 Y. Wang, L. Chen, D. Y. Ren, Z. X. Feng, L. Y. Zhang, Y. F. Zhong, M. Y. Jin, F. W. Xu, C. Y. Feng, Y. Z. Du and W. Q. Tan, *Mater. Today Bio*, 2022, **15**, 100320.
- 2 Z. G. Wu, W. Zhou, W. J. Deng, C. L. Xu, Y. Cai and X. Y. Wang, *ACS Appl. Mater. Interfaces*, 2020, **12**, 20307–20320.
- 3 Z. W. Deng, M. H. Li, Y. Hu, Y. He, B. L. Tao, Z. Yuan, R. Wang, M. W. Chen, Z. Luo and K. Y. Cai, *Chem. Eng. J.*, 2021, **420**, 129668.
- 4 Y. W. Xi, J. Ge, M. Wang, M. Chen, W. Niu, W. Cheng, Y. M. Xue, C. Lin and B. Lei, *ACS Nano*, 2020, **14**, 2904–2916.
- 5 S. Deng, J. W. Long, X. J. Dai, G. Wang and L. Zhou, *ACS Appl. Nano Mater.*, 2023, **6**, 1817–1827.
- 6 J. He, M. Shi, Y. Liang and B. Guo, *Chem. Eng. J.*, 2020, **394**, 124888.
- 7 Y. Z. Bu, L. C. Zhang, J. H. Liu, L. H. Zhang, T. T. Li, H. Shen, X. Wang, F. Yang, P. F. Tang and D. C. Wu, *ACS Appl. Mater. Interfaces*, 2016, **8**, 12674–12683.
- 8 Z. Yuan, C. C. Lin, Y. He, B. L. Tao, M. W. Chen, J. X. Zhang, P. Liu and K. Y. Cai, *ACS Nano*, 2020, **14**, 3546–3562.
- 9 K. Lv, G. W. Li, X. J. Pan, L. X. Liu, Z. H. Chen, Y. Zhang, H. Xu and D. Ma, *Adv. Healthcare Mater.*, 2023, **12**, 2300247.
- 10 Y. N. Liu, Y. Q. Xiao, Y. Y. Cao, Z. R. Guo, F. Li and L. Wang, *Adv. Funct. Mater.*, 2020, **30**, 2003196.
- 11 Z. Y. Guo, Z. Z. Zhang, N. Zhang, W. X. Gao, J. Li, Y. J. Pu, B. He and J. Xie, *Bioact. Mater.*, 2022, **15**, 203–213.
- 12 B. H. Zhao, H. Wang, W. J. Dong, S. W. Cheng, H. S. Li, J. L. Tan, J. Y. Zhou, W. F. He, L. L. Li, J. X. Zhang, G. X. Luo and W. Qian, *J. Nanobiotechnol.*, 2020, **18**, 59.
- 13 Q. Gao, X. Zhang, W. Y. Yin, D. Q. Ma, C. J. Xie, L. R. Zheng, X. H. Dong, L. Q. Mei, J. Yu, C. Z. Wang, Z. J. Gu and Y. L. Zhao, *Small*, 2018, **14**, 1802290.
- 14 S. Liang, X. R. Deng, Y. Chang, C. Q. Sun, S. Shao, Z. X. Xie, X. Xiao, P. A. Ma, H. Y. Zhang, Z. Y. Cheng and J. Lin, *Nano Lett.*, 2019, **19**, 4134–4145.
- 15 Q. Xin, H. Shah, A. Nawaz, W. J. Xie, M. Z. Akram, A. Batool, L. Q. Tian, S. U. Jan, R. Boddula, B. D. Guo, Q. Liu and J. R. Gong, *Adv. Mater.*, 2019, **31**, 1804838.
- 16 Y. Y. Xu, S. Y. Chen, Y. X. Zhang, C. Wu, L. Li, X. F. Hu, J. Y. Zhang and Y. B. Wang, *J. Mater. Chem. B*, 2023, **11**, 7069–7093.
- 17 L. P. Zhang, Y. Geng, L. J. Li, X. F. Tong, S. Liu, X. M. Liu, Z. M. Su, Z. G. Xie, D. X. Zhu and M. R. Bryce, *Chem. Sci.*, 2021, **12**, 5918–5925.
- 18 Y. X. Xing, J. X. Zhang, F. Chen, J. J. Liu and K. Y. Cai, *Nanoscale*, 2017, **9**, 8781–8790.
- 19 Z. Q. Wang, L. C. Wang, N. Prabhakar, Y. X. Xing, J. M. Rosenholm, J. X. Zhang and K. Y. Cai, *Acta Biomater.*, 2019, **86**, 416–428.
- 20 X. Y. Lv, Y. Xu, X. H. Ruan, D. L. Yang, J. J. Shao, Y. L. Hu, W. J. Wang, Y. Cai, Y. X. Tu and X. C. Dong, *Acta Biomater.*, 2022, **146**, 107–118.
- 21 C. G. Wu, J. L. Liang, X. Wang, X. Y. Zhou, X. Cai, J. Xu, M. Wang, W. B. Wang, D. Ma and W. Xue, *Sci. China: Chem.*, 2021, **64**, 1796–1810.
- 22 Z. Yuan, B. L. Tao, Y. He, C. Y. Mu, G. H. Liu, J. X. Zhang, Q. Liao, P. Liu and K. Y. Cai, *Biomaterials*, 2019, **223**, 119479.
- 23 M. Li, L. Q. Li, K. Su, X. M. Liu, T. J. Zhang, Y. Q. Liang, D. D. Jing, X. J. Yang, D. Zheng, Z. D. Cui, Z. Y. Li, S. L. Zhu, K. W. K. Yeung, Y. F. Zheng, X. B. Wang and S. L. Wu, *Adv. Sci.*, 2019, **6**, 1900599.
- 24 D. Wu, X. H. Duan, Q. Q. Guan, J. Liu, X. Yang, F. Zhang, P. Huang, J. Shen, X. T. Shuai and Z. Cao, *Adv. Funct. Mater.*, 2019, **29**, 1900095.
- 25 C. H. Su, W. P. Li, L. C. Tsao, L. C. Wang, Y. P. Hsu, W. J. Wang, M. C. Liao, C. L. Lee and C. S. Yeh, *ACS Nano*, 2019, **13**, 4290–4301.
- 26 D. O. Schairer, J. S. Chouake, J. D. Nosanchuk and A. J. Friedman, *Virulence*, 2012, **3**, 271–279.
- 27 H. F. Ma, Y. Z. Tang, F. Rong, K. Wang, T. J. Wang and P. Li, *Bioact. Mater.*, 2023, **27**, 154–167.
- 28 W. K. Liu, X. L. Song, W. Liu, Q. Lin, R. Xu, H. Li, W. Xue and S. M. Yu, *Chem. Mater.*, 2022, **34**, 10606–10622.
- 29 G. W. Li, S. M. Yu, W. Xue, D. Ma and W. Zhang, *Chem. Eng. J.*, 2018, **347**, 923–931.
- 30 J. H. He, Z. L. Li, J. X. Wang, T. Y. Li, J. Y. Chen, X. L. Duan and B. L. Guo, *Composites, Part B*, 2023, **266**, 110985.
- 31 J. Fan, Q. J. He, Y. Liu, F. W. Zhang, X. Y. Yang, Z. Wang, N. Lu, W. P. Fan, L. S. Lin, G. Niu, N. Y. He, J. B. Song and X. Y. Chen, *ACS Appl. Mater. Interfaces*, 2016, **8**, 13804–13811.
- 32 G. H. Liu, L. Wang, Y. He, L. C. Wang, Z. W. Deng, J. J. Liu, D. Peng, T. Ding, L. Lu, Y. Ding, J. X. Zhang, P. Liu and K. Y. Cai, *Adv. Healthcare Mater.*, 2021, **10**, 2101476.
- 33 K. M. Rao, K. B. Narayanan, U. T. Uthappa, P. H. Park, I. Choi and S. S. Han, *Pharmaceutics*, 2022, **14**, 1028.
- 34 H. Yu, Q. H. Xiao, G. L. Qi, F. X. Chen, B. Y. Tu, S. Zhang, Y. P. Li, Y. Chen, H. Yu and P. Duan, *Front. Bioeng. Biotechnol.*, 2022, **10**, 855013.
- 35 Q. L. Cheng, Z. H. Wang, S. M. Hu, Y. Y. Peng, R. Zhu, L. T. Zhang, J. B. Li and R. Narain, *J. Mater. Chem. B*, 2023, **11**, 7228–7238.
- 36 X. H. Huang, L. Tang, L. Xu, Y. Zhang, G. Y. Li, W. L. Peng, X. L. Guo, L. Zhou, C. J. Liu and X. C. Shen, *J. Mater. Chem. B*, 2022, **10**, 7717–7731.
- 37 Y. Meng, L. J. Chen, Y. Chen, J. Y. Shi, Z. Zhang, Y. W. Wang, F. Wu, X. W. Jiang, W. Yang, L. Zhang, C. C. Wang, X. F. Meng, Y. L. Wu and W. B. Bu, *Nat. Commun.*, 2022, **13**, 7353.
- 38 H. L. Wang, X. Nie, W. You, W. Q. Huang, G. Chen, F. Gao, L. Xia, L. Zhang, L. H. Wang, A. Z. Shen, K. L. Wu, S. G. Ding and Y. Z. You, *ACS Appl. Mater. Interfaces*, 2021, **13**, 56838–56849.

- 39 X. Zhao, B. L. Guo, H. Wu, Y. P. Liang and P. X. Ma, *Nat. Commun.*, 2018, **9**, 2784.
- 40 S. Kim, Z. K. Cui, J. B. Fan, A. Fartash, T. L. Aghaloo and M. Lee, *J. Mater. Chem. B*, 2016, **4**, 5289–5298.
- 41 J. X. Huang, S. Wang, Y. X. Xing, W. Zhou, J. X. Zhang and K. Y. Cai, *Macromol. Rapid Commun.*, 2019, **40**, 1900263.
- 42 S. F. Zhao, L. Zhang, L. Deng, J. Ouyang, Q. Q. Xu, X. Y. Gao, Z. L. Zeng and Y. N. Liu, *Small*, 2021, **17**, 2103003.
- 43 P. P. Deng, X. Liang, F. X. Chen, Y. Chen and J. P. Zhou, *Appl. Mater. Today*, 2022, **26**, 101362.
- 44 H. Y. Zhang, X. L. Li, H. B. Kang and X. Y. Peng, *Meat Sci.*, 2022, **188**, 108779.
- 45 Y. J. Jing, Y. J. Diao and X. Q. Yu, *React. Funct. Polym.*, 2019, **135**, 16–22.
- 46 J. Liu, J. F. Lu, J. Kan and C. H. Jin, *Int. J. Biol. Macromol.*, 2013, **62**, 321–329.
- 47 X. L. Qi, Y. J. Huang, S. Y. You, Y. J. Xiang, E. Y. Cai, R. T. Mao, W. H. Pan, X. Q. Tong, W. Dong, F. F. Ye and J. L. Shen, *Adv. Sci.*, 2022, **9**, 2106015.
- 48 P. Zhao, Y. Zhang, X. A. Chen, C. Xu, J. Z. Guo, M. G. Deng, X. W. Qu, P. S. Huang, Z. J. Feng and J. M. Zhang, *Adv. Sci.*, 2023, **10**, 2206585.
- 49 J. Qu, X. Zhao, Y. P. Liang, T. L. Zhang, P. X. Ma and B. L. Guo, *Biomaterials*, 2018, **183**, 185–199.
- 50 Z. P. Ni, H. J. Yu, L. Wang, X. W. Liu, D. Shen, X. Chen, J. Y. Liu, N. Wang, Y. D. Huang and Y. Sheng, *Adv. Healthcare Mater.*, 2022, **11**, 2101421.
- 51 R. Y. Bai, H. M. Yong, X. Zhang, J. Liu and J. Liu, *Int. J. Biol. Macromol.*, 2020, **143**, 49–59.
- 52 J. Liu, J. F. Lu, J. Kan, Y. Q. Tang and C. H. Jin, *Int. J. Biol. Macromol.*, 2013, **62**, 85–93.
- 53 C. H. Wang, W. S. Liu, J. F. Sun, G. G. Hou, Q. Chen, W. Cong and F. Zhao, *Int. J. Biol. Macromol.*, 2016, **84**, 418–427.
- 54 R. R. Guo, Y. Tian, Y. J. Wang and W. L. Yang, *Adv. Funct. Mater.*, 2017, **27**, 1606398.
- 55 Y. Xu, H. Ren, J. W. Liu, Y. L. Wang, Z. J. Meng, Z. J. He, W. J. Miao, G. G. Chen and X. M. Li, *Nanoscale*, 2019, **11**, 5474–5488.
- 56 Z. J. Du, Y. Mao, P. F. Zhang, J. Hu, J. J. Fu, Q. J. You and J. Yin, *ACS Appl. Mater. Interfaces*, 2021, **13**, 35518–35532.
- 57 F. Rizzo and N. S. Kehr, *Adv. Healthcare Mater.*, 2021, **10**, 2001341.
- 58 Y. T. Yang, Y. P. Liang, J. Y. Chen, X. L. Duan and B. L. Guo, *Bioact. Mater.*, 2022, **8**, 341–354.
- 59 H. Q. Tan, D. W. Jin, J. J. Sun, J. L. Song, Y. Lu, M. Yin, X. Chen, X. Qu and C. S. Liu, *Bioact. Mater.*, 2021, **6**(3), 905–917.
- 60 M. X. Chen, T. J. Chen, J. F. Bai, S. Y. He, M. Y. Luo, Y. L. Zeng, W. Z. Peng, Y. C. Zhao, J. X. Wang, X. D. Zhu, W. Zhi, J. Weng, K. Zhang and X. D. Zhang, *Adv. Healthcare Mater.*, 2023, 2301560.
- 61 Y. Wei, L. J. Xiang, P. H. Zhu, Y. Y. Qian, B. X. Zhao and G. Chen, *Chem. Mater.*, 2021, **33**, 8623–8634.
- 62 J. Y. Mo, Y. H. Dai, C. Zhang, Y. S. Zhou, W. B. Li, Y. X. Song, C. Y. Wu and Z. A. K. Wang, *Mater. Horiz.*, 2021, **8**, 3409–3416.
- 63 G. H. Yang, Z. K. Zhang, K. F. Liu, X. X. Ji, P. Fatehi and J. C. Chen, *J. Nanobiotechnol.*, 2022, **20**, 312.
- 64 B. Balakrishnan, M. Mohanty, P. R. Umashankar and A. Jayakrishnan, *Biomaterials*, 2005, **26**, 6335–6342.
- 65 A. F. Halbus, T. S. Horozov and V. N. Paunov, *ACS Appl. Mater. Interfaces*, 2019, **11**, 12232–12243.
- 66 A. Galstyan, R. Schiller and U. Dobrindt, *Angew. Chem., Int. Ed.*, 2017, **56**, 10362–10366.
- 67 Z. J. Xu, S. Y. Han, Z. P. Gu and J. Wu, *Adv. Healthcare Mater.*, 2020, **9**, 1901502.
- 68 H. C. Flemming, J. Wingender, U. Szewzyk, P. Steinberg, S. A. Rice and S. Kjelleberg, *Nat. Rev. Microbiol.*, 2016, **14**, 563–575.
- 69 Y. Liu, L. Q. Shi, L. Z. Su, H. C. van der Mei, P. C. Jutte, Y. J. Ren and H. J. Busscher, *Chem. Soc. Rev.*, 2019, **48**, 428–446.
- 70 Z. W. Chen, H. W. Ji, C. Q. Liu, W. Bing, Z. Z. Wang and X. G. Qu, *Angew. Chem., Int. Ed.*, 2016, **55**, 10732–10736.
- 71 Y. X. Liu, S. Chakraborty, C. Direksilp, J. M. Scheiger, A. A. Popova and P. A. Levkin, *Mater. Today Bio*, 2021, **12**, 100153.
- 72 J. Z. Yi, S. Y. Wu, S. W. Tan, Y. F. Qin, X. Wang, J. Jiang, H. L. Liu and B. Wu, *Cell Death Discov.*, 2021, **7**, 374.
- 73 P. F. Zhuang, K. Li, D. Y. Li, H. X. Qiao, Y. F. E, M. Q. Wang, J. C. Sun, X. F. Mei and D. Li, *Nanoscale Res. Lett.*, 2021, **16**, 121.
- 74 C. A. Guo, Y. Wu, W. L. Li, Y. Wang and Q. Q. Kong, *ACS Appl. Mater. Interfaces*, 2022, **14**, 30480–30492.
- 75 J. E. Cun, Y. Pan, Z. Z. Zhang, Y. Lu, J. H. Li, Q. Q. Pan, W. X. Gao, K. Luo, B. He and Y. J. Pu, *Biomaterials*, 2022, **287**, 121687.
- 76 Y. Yang, M. Li, G. Pan, J. Chen and B. Guo, *Adv. Funct. Mater.*, 2023, **33**, 2214089.
- 77 D. Y. Chen, X. Y. Zhou, L. M. Chang, Y. Wang, W. J. Li and J. L. Qin, *Biomacromolecules*, 2021, **22**, 2272–2283.
- 78 J. Zhu, F. X. Li, X. L. Wang, J. Y. Yu and D. Q. Wu, *ACS Appl. Mater. Interfaces*, 2018, **10**, 13304–13316.
- 79 S. Yang, X. M. Li, P. Liu, M. L. Zhang, C. Wang and B. Zhang, *ACS Biomater. Sci. Eng.*, 2020, **6**, 4666–4676.
- 80 H. B. Yuan, L. Chen and F. F. Hong, *ACS Appl. Mater. Interfaces*, 2020, **12**, 3382–3392.
- 81 C. Y. Liu, W. H. Yao, M. Tian, J. N. Wei, Q. L. Song and W. H. Qiao, *Biomaterials*, 2018, **179**, 83–95.
- 82 Y. Wang, H. D. Shi, H. L. Zhang, Y. Y. Chen, B. Ren, Q. Tang, Q. Sun, Q. L. Zhang and J. G. Liu, *Adv. Healthcare Mater.*, 2023, **12**, 2300568.